

# Magnetic Atmospheres and Circumstellar Interaction in J1901+1458: Revisiting the Most Compact White Dwarf Merger Remnant in the light of new UV and X-ray data

## A new class of white dwarf merger remnants with X-ray emission

Aayush Desai<sup>1</sup>, Ilaria Caiazzo<sup>1,2</sup>, Stephane Vennes<sup>3</sup>, Adela Kawka<sup>4</sup>, Tim Cunningham<sup>5</sup>, Gauri Kotiwale<sup>1</sup>, Andrei A. Cristea<sup>1</sup>, John C. Raymond<sup>5</sup>, Maria Camisassa<sup>19</sup>, Leandro G. Althaus<sup>18</sup>, J. J. Hermes<sup>7</sup>, Iris Traulsen<sup>19</sup>, James Fuller<sup>8</sup>, Jeremy Heyl<sup>6</sup>, Jan van Roestel<sup>9</sup>, Kevin B. Burdge<sup>10</sup>, Antonio C. Rodriguez<sup>2</sup>, Ingrid Pelisoli<sup>11</sup>, Boris T. Gänsicke<sup>11</sup>, Paula Szkody<sup>13</sup>, Sumit K. Maheshwari<sup>17</sup>, Zachary P. Vanderbosch<sup>2</sup>, Andrew Drake<sup>2</sup>, Lilia Ferrario<sup>3</sup>, Dayal Wickramasinghe<sup>3</sup>, Stephen Justham<sup>14</sup>, Ruediger Pakmor<sup>14</sup>, Kareem El-Badry<sup>2</sup>, Thomas Prince<sup>2</sup>, S. R. Kulkarni<sup>2</sup>, Matthew J. Graham<sup>2</sup>, Ben Rusholme<sup>15</sup>, Russ R. Laher<sup>15</sup>, and Josiah Purdum<sup>16</sup>

(Affiliations can be found after the references)

### ABSTRACT

Double-degenerate white dwarf (WD) mergers can exhibit extreme magnetic fields exceeding  $10^8$  G and rapid rotation, but their spectral-energy distributions and high-energy emission mechanisms remain poorly characterised. ZTF J1901+1458 stands out as the most compact and strongly magnetised object discovered in this class to date. Intriguingly, recent Chandra observations have revealed that the white dwarf is also a source of soft X-ray emission, too bright and hard to be of photospheric origin. We analyse new phase-resolved UV spectroscopy from the Hubble Space Telescope, combined with optical and near-infrared photometry and spectroscopy, with newly developed magnetic atmosphere models to determine its effective temperature, radius, mass, average surface magnetic field strength, and cooling age. Our results demonstrate that the spectral break at  $\approx 3000$  Å, observed in several highly magnetised WDs, is well-reproduced by our new models, which take into account the effect of magnetic opacities on the structure of the atmosphere. Our best-fit parameters for the WD yield a cooler effective temperature ( $T_{\text{eff}} = 28,015 \pm 20$  K) and larger radius ( $2630 \pm 10$  km) than previously reported. Furthermore, the near-infrared data exclude the presence of a stellar or brown dwarf companion hotter than  $\approx 700$  K. We also jointly analyse the previously published *Chandra*/ACIS-I data and new *XMM-Newton*/EPIC X-ray spectra. The faint X-ray emission,  $L_X = (1.3 \pm 0.2) \times 10^{27}$  erg s<sup>-1</sup>, is highly pulsed on the rotation period of the WD, and the soft spectrum can be modelled by a power law model with photon index  $\Gamma = 2.9^{+0.4}_{-0.3}$ . We suggest that the X-rays are powered by accretion or via the interaction of the WD magnetosphere with circumstellar material. If the rapidly rotating magnetic field could power a weak wind along open field lines, material could be extracted directly from the surface of the WD. Alternatively, a low level of accretion of fallback material from the past merger event or the tidal disruption of a planetary body are possible sources of CSM.

**Key words.** White dwarfs – Accretion, accretion disks – Line: profiles – Circumstellar matter – Stars: variables: general – Stars: magnetic field – Stars: winds, outflows – X-rays: stars

### 1. Introduction

White dwarfs, the compact remnants left behind by stars like our Sun, are key laboratories for exploring the outcomes of stellar evolution, particularly through the dramatic scenario of double-degenerate mergers. When two WDs spiral into each other and merge, they can produce highly magnetised, rapidly rotating remnants whose extreme physical conditions push the boundaries of known stellar physics (see e.g. Wickramasinghe & Ferrario 2000; García-Berro et al. 2012). Under certain conditions, such merger events can significantly enhance magnetic fields through dynamo action, spin up the remnant to rotation periods of minutes, and create ultra-massive WDs that approach the Chandrasekhar limit (see e.g. Tout et al. 2008; García-Berro et al. 2012; Schwab 2021b; Pakmor et al. 2024; Munday et al. 2025a,b). Despite the theoretical predictions, only a handful of objects with definitive merger signatures have been identified (Vennes et al. 2003; Caiazzo et al. 2021; Jewett et al. 2024; Sahu et al. 2025).

The study of these merger products provides crucial insights into magnetic field amplification, rotational evolution, accretion processes, and binary evolution. The strong field threading the surface of these WDs affects the structure and opacities of their atmospheres, and might affect their evolution; therefore, the development of atmosphere models that take into account the effects of the strong field is paramount to model these sources and understand their physical properties. Previous studies of extremely magnetised WDs ( $B > 100$  MG) have shown that their spectral energy distribution differs dramatically from non-magnetised ones, especially in the ultraviolet range (Green & Liebert 1981; Schmidt et al. 1986; Gänsicke et al. 2001). We here present new, state-of-the-art atmosphere models that include the effect of a varying magnetic field on the surface of magnetised WDs and can reproduce the observed spectra of these ultra-magnetised objects.

Another key factor in the evolutionary history of merger remnants is fallback accretion. Numerical simulations of double WD mergers show that right after the merger the remnant is surrounded by a thick disk and extended tidal tails, and while

some of the material is either ejected or rapidly accreted, material on eccentric orbits is accreted on longer timescales, supplying a low-level but sustained accretion flow (see e.g. [Guerero et al. 2004](#); [Rosswog 2007](#); [Lorén-Aguilar et al. 2009](#); [Dan et al. 2014](#)). This fallback rate is initially high but decays over time, releasing gravitational potential energy that can heat the remnant’s outer layers and power high-energy emission. Such a mechanism may also affect the spin evolution and thermal structure of the remnant over extended timescales and would provide another mechanism to identify merger remnants (see e.g. [Rueda et al. 2019](#); [Sousa et al. 2022](#); [Yang et al. 2022](#)). However, until recently, no signs of long-term accretion from fallback have been observed in a merger remnant.

ZTF J1901+1458 (hereafter J1901) has emerged as a cornerstone object in the field of WD merger remnants. Discovered in 2021 ([Caiazzo et al. 2021](#), hereafter C21) as a variable source in the Zwicky Transient Facility archive ([Bellm et al. 2019](#); [Graham et al. 2019](#); [Dekany et al. 2020](#); [Masci et al. 2019](#)), J1901 was immediately recognised as extreme. It was reported to have a diminutive radius of only  $\approx 2140$  km (comparable to Earth’s Moon) and a mass in the range  $1.327\text{--}1.365 M_{\odot}$ , with an extremely short rotation period of 6.94 minutes. Its surface magnetic field was inferred to reach 600–900 MG, placing it among the most strongly magnetised WDs known.

As typical WDs exhibit rotation periods of hours to days (see e.g. [Koester et al. 1998](#); [Charpinet et al. 2009](#); [Hermes et al. 2017](#)), the rapid rotation rate of J1901, combined with its extremely high mass and intense magnetic field, provides strong evidence that the star was born in a double-degenerate merger. Additionally, the radius and mass derived in the discovery paper imply that J1901 is perilously close to the Chandrasekhar limit. C21 also noted that electron captures could, in principle, bring J1901 close to instability, and outlined a scenario in which, at the high densities reached in the WD core  $^{23}\text{Na}$  atoms can undergo inverse beta decay, and therefore capture an electron to produce  $^{23}\text{Ne}$  atoms. At the high densities considered, the reverse  $\beta^-$  decay is blocked, so the process does not operate as a reversible Urca cycle and instead results in a net decrease of the electron fraction  $Y_e$ , reducing the pressure and leading the core to shrink. This change could then bring the core to the density thresholds for captures on  $^{24}\text{Mg}$  and  $^{20}\text{Ne}$ , which further reduce  $Y_e$  and might make J1901 unstable to collapse. J1901 would thus be a valuable case to investigate the interplay between chemical stratification, neutrino cooling, and the ultimate stability of ultra-massive WDs.

The initial characterisation of J1901, however, was based only on optical and near UV data, and the estimates for the temperature and radius of the star (and thus of the mass and age) were obtained by modelling the observed spectral energy distribution (SED) of the WD with non-magnetic atmosphere models. As we mentioned above, and as we show in detail in this work, magnetic fields have an important effect on the emission from ultra-magnetised WDs, both in the location and strength of the absorption lines and in the shape of the overall SED; therefore, these estimates of J1901 should be revisited. For this reason, we undertook a comprehensive follow-up campaign of J1901. We leveraged ultraviolet observations (from the Hubble Space Telescope; details in Section 2) alongside new optical and infrared photometry and spectroscopy to refine J1901’s fundamental parameters and constrain the presence of a stellar or sub-stellar companion (Section 3). The inclusion of ultraviolet spectroscopy is especially valuable: at the effective temperature of J1901 ( $\approx 28,000$  K), a significant portion of the WD’s flux emerges in the UV, thus providing a tight handle on the effective

temperature, radius, and interstellar extinction that optical data alone cannot well constrain. Most importantly, for the characterisation, we employ a new set of magnetic atmosphere models that include, for the first time, the effect of magnetic opacities on the structure of the atmosphere and are able to reproduce the full SED of ultramagnetised WDs.

Another focus of this work is the high-energy emission of J1901. The WD has been the target of two X-ray campaigns with Chandra (Proposal ID 24200244, PI Safdi) and XMM-Newton (ObsID 0922750101, PI Traulsen) to search for the signature of emission from axion-like particles. It is predicted that axions could be produced in the dense and hot cores of WDs from electron bremsstrahlung ([Ning et al. 2025](#)) and nuclear transitions ([Fleury et al. 2023](#)), and could afterwards be converted into high-energy photons in the WDs’ magnetosphere ([Dessert et al. 2019, 2022](#)). Although no evidence for axion bremsstrahlung emission was discovered in the Chandra data ([Ning et al. 2025](#)), the X-ray flux shows a strong excess with respect to the expected photospheric emission of the WD based on its measured temperature and radius. We here re-analyse the Chandra data for J1901 and present the new XMM-Newton data, performing both a timing and spectroscopic analysis (Section 3.7). In the absence of a mass-transferring companion, we present several alternative explanations for the origin of the X-ray emission.

Clues on the nature of J1901 and its high-energy emission could be drawn from a comparison with a very similar WD merger remnant that we recently discovered to have analogous X-ray emission properties, and which presents additional evidence of circumstellar material trapped in its magnetosphere. We present this discovery in a companion paper ([Cristea et al. 2025](#)): the WD ZTF J2008+4449 exhibits an unusually short rotation period of 6.6 minutes and a strong surface magnetic field of  $\sim 5 \times 10^8$  G, similar properties to J1901 that also suggest an origin as a WD merger remnant. Also, a targeted observation with XMM-Newton of ZTF J2008+4449 revealed soft X-ray emission with a remarkably similar spectral shape to J1901. Additionally, in this system, we detected emission lines of hydrogen that vary in Doppler velocities with the rotation period of the WD, indicating the presence of circumstellar material likely trapped in corotation with the WD by the strong magnetic field, and a significant increase in spin period ( $\dot{P} \approx 2 \times 10^{-12}$  s/s), indicating that some material is leaving the system, carrying away angular momentum. As these two systems are among the most rapidly rotating and most highly magnetised WDs known that are not part of a binary, they might represent a new class of merger remnants interacting with circumstellar material.

The paper is structured as follows: Section 2 describes the observations and data reduction. Section 3 presents the analysis and results. Section 4 discusses the implications of our findings. Section 5 details a comparison with ZTF J2008+4449 and other known merger remnants and Section 6 summarises our results.

## 2. Observations

In this section, we describe the different datasets that we analyse in this paper. In particular, we have obtained new UV spectroscopy, as well as optical and infrared photometry and infrared spectroscopy, and we have analysed the publicly available X-ray observations. To properly phase the observations between different epochs, we converted all times into modified Julian Date (MJD) in the Barycentric Dynamical Time (TDB) scale.

## 2.1. HST data

J1901 was observed (programme ID **16753**, [Caiazzo et al. 2021](#)) with the Cosmic Origins Spectrograph (COS) and Space Telescope Imaging Spectrograph ([Green et al. 2011](#); [Woodgate et al. 1998](#)) on the Hubble Space Telescope (HST). The details of the observations are summarised in Table A.1. The low-resolution grating G140L, with central wavelength 800 Å, was used on COS, yielding a spectral coverage over the range  $\approx 900\text{--}1900$  Å at a resolving power of  $R \approx 2000$ . For STIS, we used the G230L NUV MAMA grating, covering the range  $\approx 1600\text{--}3000$  Å with a resolving power of  $R \approx 500$ . We reduced the data using the default CalCOS and CalSTIS pipelines for COS and STIS, respectively ([Kaiser et al. 2008](#); [Hulbert & Hodge 1997](#)). The effective pixels of the COS XDL (cross-delay line camera of the FUV channel) highly oversample the spectral resolution with about six bins per resolution element<sup>1,2</sup>. We re-bin the flux and its error for each phase-resolved spectrum using the *SpectRes* code (see [Carnall 2017](#)).

The averaged spectrum over the entire observation for COS (1100–1800 Å) and STIS (1800–3100 Å) is shown in the upper left panel of Fig. 1. Broad, weak absorption features can be seen across the STIS spectrum. In the COS spectrum, we can see two strong absorption features at 1096 and 1342 Å. As shown in the lower panel, these features correspond to absorption lines of hydrogen, split into Zeeman components and shifted by the high magnetic field ([Schimeczek & Wunner 2014](#)). In particular, the line at 1342 Å corresponds to a Lyman  $\alpha$  component ( $1s0 \rightarrow 2p0$ ), while the line at 1096 Å is a blend of a permitted Ly  $\alpha$  component ( $1s0 \rightarrow 2p-1$ ) and a forbidden Ly  $\beta$  component ( $1s0 \rightarrow 3d-2$ ); the location of the lines indicate an average surface field strength of  $B_{\text{avg}} \approx 7 \times 10^8$  G.

Since the observations were taken in time-tag mode, we phase-bin the spectra on the 6.9-minute period using the default *splittag* and *inttag* Python functions. All timestamps were converted to the barycentric dynamical time (TDB) system using an adapted version of the *barycorrpy* routine. The bottom panel of Fig. 1 shows the phase-resolved spectra over two periods. We can see a strong sinusoidal variation in the continuum across all wavelengths, with significant shifts in phase as a function of wavelength (the minimum in brightness occurs at different phases at different wavelengths). This is also highlighted by the phase-folded light curves extracted in three FUV bands (COS; C1–C3) and three NUV bands (STIS; S1–S3), showing a sinusoidal variation out of phase between the different bands (middle right panel). We can also see that the amplitude (peak-to-peak) of variation increases at bluer wavelengths, from 4% in the reddest band of STIS to 12% in the bluest band of COS.

Furthermore, we see some small variations in the two strong absorption lines as a function of phase. In particular, we see a shift in wavelength of both components of about 2 Å and a very subtle variation in depth. To quantify these variations as a function of phase, we fit two Gaussians to the two lines at 1096 and 1342 Å, and we show the results in Fig. 2. This figure shows the variation of the fitted strength (amplitude of the Gaussian), central wavelength (mean), and width (sigma) of the absorption features versus rotational phase. The values on the y-axes are sub-

tracted from the mean values over the phases. The central panel in Fig. 2 shows that the centroids of the two features shift in wavelength in phase with each other, likely due to a variation in magnetic field strength over the surface of the WD. From the *spaghetti* plot in Fig. 1, we can see that the  $1s0 \rightarrow 2p0$  Lyman  $\alpha$  component and the  $1s0 \rightarrow 3d-2$  forbidden transition of Lyman  $\beta$  vary with field in a similar fashion, while the  $\pi$  component of the Lyman  $\alpha$  transition varies much faster as a function of the field strength in that regime. It is therefore likely that the 1100 Å line is dominated by the  $1s0 \rightarrow 3d-2$  forbidden transition. On the other hand, the width of the 1100 Å line varies significantly more with phase than that of the 1342 Å line (right-most panel in Fig. 2), highlighting the contribution of the  $\pi$  component of Ly $\alpha$  being extremely sensitive to the magnetic field strength in that region.

## 2.2. Photometric data

To model the SED of the WD, we employ available photometric data from the Pan-STARRS PS1 survey ([Chambers et al. 2019](#)). Since the reported errors are less than the intrinsic photometric variation, we use an error of 0.02 magnitudes instead to take into account the error induced by variability. These are the errors reported in Table. 1.

We supplement our optical photometry with light curves from the ZTF survey ([Masci et al. 2019](#); [Bellm et al. 2019](#); [Dekany et al. 2020](#); [Graham et al. 2019](#)) in the  $g$ ,  $r$  and  $i$  bands. The ZTF light curves are available from the ZTF archive<sup>3</sup> and were extracted using the *ztfquery* Python package ([Rigault 2018](#)). We also acquired high-speed photometric observations in the  $g$  and  $r$  filters using the Caltech High-speed Multi-color camera (CHIMERA; [Harding et al. 2016](#)) mounted on the 200-inch Hale Telescope at Palomar Observatory in three different nights: August 18 2020, April 24 2025 and May 30 2025. The single exposure time for each image was 3 s, and the total exposure time for each night was 80, 30 and 75 minutes, respectively. The absolute local time of each exposure was recorded with millisecond precision using a GPS receiver. Standard bias subtraction and flat-fielding procedures were applied to the images. Aperture photometry was then performed using the ULTRACAM pipeline ([Dhillon et al. 2007](#)), with differential light curves constructed relative to a single non-variable comparison star. We also obtained high-speed photometry in the  $u$  band using LightSpeed ([Burdge in prep](#)), which was temporarily mounted atop the Hale telescope for testing on the night of October 27th 2024. The total exposure time was 40 minutes, while the single exposure time for each image was 1 s. The light curve was obtained upon reducing the images using a bespoke reduction pipeline developed for LightSpeed ([Burdge in prep](#)). The CHIMERA and LightSpeed light curves, phase-folded on the spin period of the WD, are shown in Fig. 3.

Near-infrared images of the WD in the  $J$ ,  $H$  and  $K_s$  bands are available from the UKIRT Infrared Deep Sky Survey (UKIDSS) ([Lawrence et al. 2007](#)). The UKIDSS catalogue only provides calibrated images; we therefore performed aperture photometry on the available images to obtain  $J$ ,  $H$  and  $K_s$  magnitudes for J1901. We first determined the image dimensions and extracted the sky coordinates at the frame edges using the WCS header. A crossmatch with the publicly available Gaia–2MASS catalogue (V/155) (see [Fouesneau et al. 2022](#)) provided high-accuracy astrometry and proper motion data for stars within the field. The Gaia astrometric solutions were then proper-motion adjusted to

<sup>1</sup> <https://hst-docs.stsci.edu/cosihb/chapter-3-description-and-performance-of-the-cos-optics/3-2-size-of-a-resolution-element>

<sup>2</sup> Note that the FUV detector does not have physical pixels – digitised positions are derived for each count, and it is these that we consider as “pixels”

<sup>3</sup> <https://irsa.ipac.caltech.edu/Missions/ztf.html>



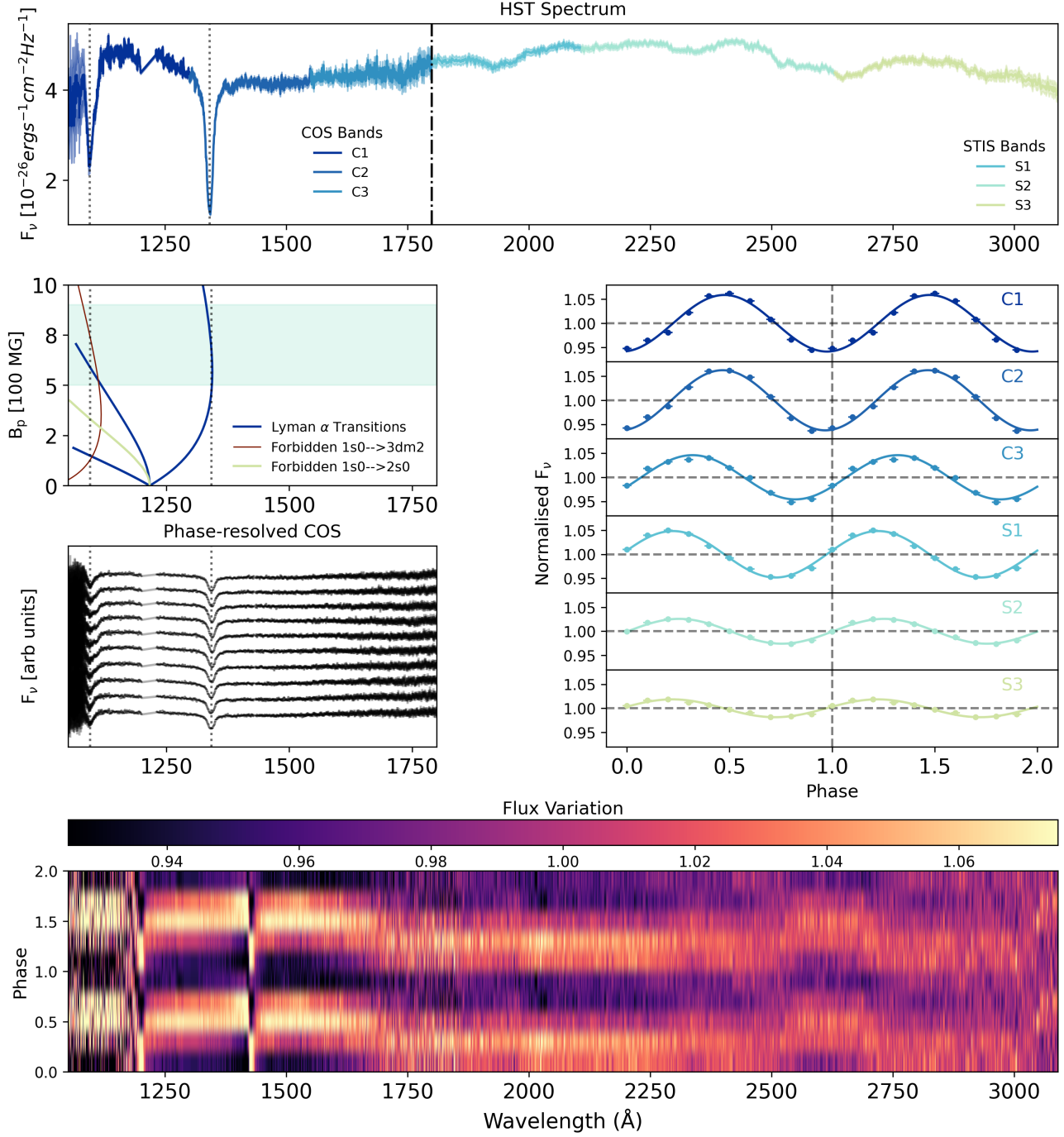


Fig. 1: COS and STIS spectra of J1901. **Top:** Phase-averaged UV spectrum of J1901. The different bands used to reconstruct the light curves are marked by their respective colours. **Middle Right:** Light curves of J1901 for the bands defined in the top panel. Each light curve is divided by its mean and placed in a panel with y-axis limits set to (0.92,1.08). The phase was calculated while fixing the amplitude and period. They are reported in units of the period. Bands 1 and of COS are  $\approx 40\text{s}$  (10%) out of phase with respect to band 3. This is corroborated by the band 1 phase of STIS. **Upper-middle Left:** Spaghetti plot showing the Lyman alpha and forbidden absorption lines detected in the COS spectrum with different magnetic field strengths on the y-axis. **Lower-middle Left:** Plot showing the normalised phase-resolved COS spectrum. The movement of the 1340 Å line over the different phases is visible. **Bottom:** Phase-resolved spectra divided by the phase-averaged spectrum and plotted over two periods. The colorbar shows the variation in flux with respect to the mean.

the UKIDSS observation epoch, and refined centroids for each source were obtained by fitting 2D Gaussians using `photutils` (see Bradley et al. 2024). Aperture photometry was performed at the corrected positions with apertures scaled to the seeing (typi-

cally  $\sim 2 \times \text{FWHM}$ ), and Poisson noise was propagated through both source and background contributions. To ensure robust flux calibration, we used reference stars with known 2MASS magnitudes and carefully accounted for background subtraction uncer-



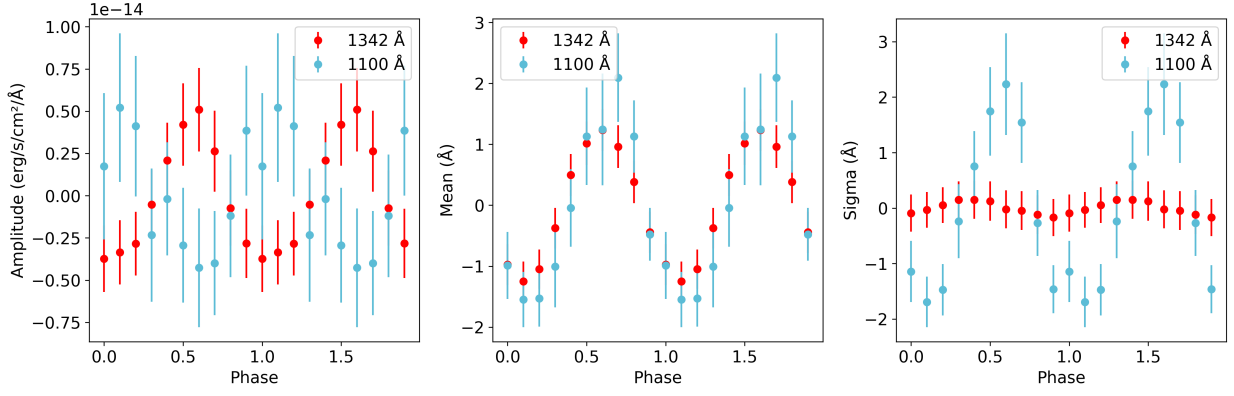


Fig. 2: Line profiles of the absorption features present at  $\approx 1096.30$  Å (blue points) and  $\approx 1342.16$  Å (red points). The y-axis in each plot represents the variation of the corresponding parameters over each phase. These are calculated by subtracting the mean (over the 10 phases) from the value of each parameter at every phase. While the amplitudes (in the leftmost figure) vary out of phase, the locations vary almost in phase.

Table 1: Optical and near-IR photometry of J1901

Filter	$\lambda_{\text{eff}}$ [Å]	Magnitude	Uncertainty
Pan-STARRS <i>g</i>	4814	15.512	0.02
Pan-STARRS <i>r</i>	6170	15.977	0.02
Pan-STARRS <i>i</i>	7525	16.275	0.02
Pan-STARRS <i>z</i>	8660	16.594	0.02
Pan-STARRS <i>y</i>	9620	16.762	0.02
UKIDSS <i>J</i>	12350	17.339	0.11
UKIDSS <i>H</i>	16500	17.765	0.14
UKIDSS <i>K<sub>s</sub></i>	21700	18.746	0.33

**Notes.** Pan-STARRS and UKIDSS magnitudes are in the AB system.

ainties using both pixel-based and area-weighted background estimates. The resulting magnitudes and errors are listed in Table 1.

### 2.3. Infrared Spectroscopy

We obtained near-infrared spectroscopy with the Folded-port InfraRed Echellette spectrograph (FIRE, [Simcoe et al. 2008, 2010](#)) on the Magellan Baade 6.5 m telescope. We observed J1901 on 15<sup>th</sup> July 2025 in the echelle mode, which provides a resolving power of  $R \approx 6000$  spanning the 1.0–2.5  $\mu\text{m}$  range. The observations were conducted with the 0.6'' slit, at parallactic angle to minimise differential atmospheric refraction. We used exposure times of 600 s, for sequences of ABAB dithers across 9 individual science exposures, with a total integration of 5400 s. We chose the Sample Up The Ramp mode for the readout in order to minimize overheads. We also obtained a standard star for telluric correction. The data was reduced using the `pypeit` package for semi-automated reduction of astronomical slit-based spectroscopy ([Prochaska et al. 2020a,b](#)). We show the FIRE spectrum in Fig. 4.

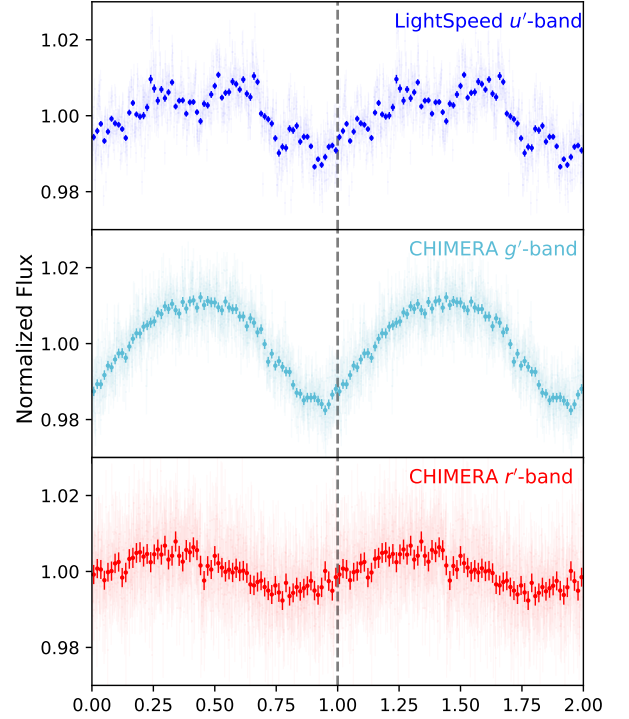


Fig. 3: LightSpeed (upper plot) and CHIMERA (lower two plots) light curve phase-folded, binned in phase and normalised to the mean of the light curve in the  $u'$ -band (upper), in the  $g'$ -band (middle) and in the  $r'$ -band (lower). The CHIMERA data was taken in 3-second exposures, while the LightSpeed in 1-second exposures.

### 2.4. X-ray data

#### 2.4.1. Chandra X-ray Observatory

J1901 was observed with the ACIS-I instrument ([Garmire et al. 2003](#)) onboard the Chandra X-ray Observatory (hereafter Chandra; [Weisskopf et al. 2000](#)) on 9th and 10th December, 2022. The observation (Proposal ID 24200244; PI Safdi) comprises three observations (ObsIDs 26496, 27596, and 27597), with exposure times ranging from 10–15 ks, with a collective total ex-

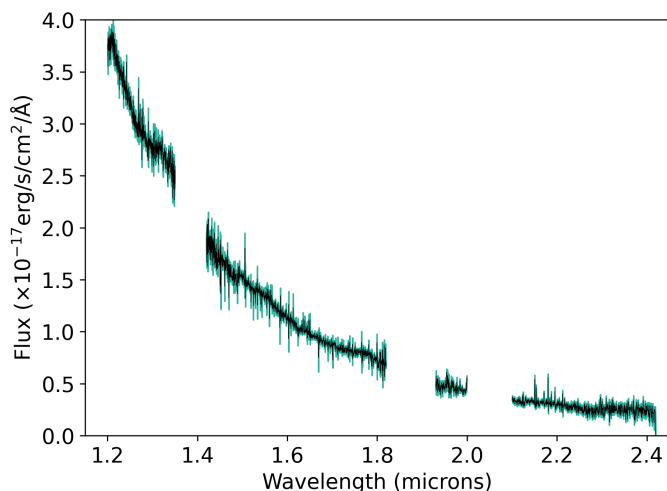


Fig. 4: Spectrum obtained from the FIRE instrument. The black line is the spectrum with the cyan region indicating the  $1\sigma$  errors. The regions with strong telluric contamination were removed from the data.

posure time of 39.3 ks. All observations were performed with the very faint mode which stores event grades in regions of  $5\times 5$  pixels, rather than the default  $3\times 3$ , and enables improved rejection of background events. We retrieved the primary and secondary data products from the Chandra Data Archive<sup>4</sup> and performed the data reduction using the software package *Chandra Interactive Analysis of Observations* (CIAO; Fruscione et al. 2006). We began the reduction by reprocessing the three observations using the `chandra_repro` tool, with standard status, grade, good time filters and very faint background cleaning. We utilised `merge_obs` to merge the three observations into a single set of events files and associated images, point spread function (PSF) maps and exposure maps. The PSF and exposure maps were generated with exposure evaluated on an energy of 0.9 keV, corresponding approximately to the median source photon energy. We extracted spectra for the source and adjacent background region using the standard procedure outlined in the CIAO documentation. The source and background circular apertures had radii of 2.0 and 80 arcsec, respectively. Bamba et al. (2024) and Ning et al. (2025) previously analysed these *Chandra* X-ray observations and reported a marginal X-ray detection (at the  $3.5\sigma$  and  $2.6\sigma$  level, respectively), finding a X-ray flux of  $\sim 10^{-15}$  erg s $^{-1}$  cm $^{-2}$ , comparable to our estimate (see Section 3.7). The first authors noted that the source detection algorithm `wavdetect` distributed within CIAO yielded no source detection at the target. We re-analyse the Chandra data, making use of the VFaint mode in which the data were taken. Around each detected event, VFaint mode stores  $5\times 5$  pixel regions, rather than the  $3\times 3$  default in Faint, which enables greater discrimination of good from bad X-ray events. Our new analysis yields a detection of an X-ray source at the expected location of our target with a significance in excess of  $6\sigma$ . We examine the significance of source detection in the ACIS science energy bands: ultrasoft (0.2–0.5 keV), soft (0.5–1.2 keV), medium (1.2–2.0 keV), hard (2.0–7.0 keV) and broad (0.5–7.0 keV). Of the standard Chandra science energy bands, we find significant detections in the medium and broad bands, with significances of  $6.5$  and  $6.9\sigma$ , respectively. The detection significance is dominated by counts in

the medium band, in which we identify 6 source counts above an estimated expected background of 0.06 counts in the 2.0 arcsec source aperture across the 39.3 ks total exposure time, based on the total background counts in an adjacent 80 arcsec aperture. All other Chandra science bands yield a detection significance less than  $3\sigma$ . These results, along with confidence limits on the source count rates determined using the Bayesian prescription of Kraft et al. (1991), are summarised in the Appendix Table B.2. Additionally, we perform a source detection using `wavdetect` on images in the soft, medium and hard energy bands. We find that in the medium band, `wavdetect` finds a source at the target location, whilst in the other two bands no source is detected. The Chandra X-ray spectral analysis is presented in Section 3.7.

#### 2.4.2. XMM-Newton

J1901 was also observed with XMM-Newton (hereafter XMM; Jansen et al. 2001) on the 21st and 22nd March, 2024 (ObsID 0922750101; PI Traulsen) with a 77.8 ks observation. In this work, we rely primarily on data from the European Photon Imaging Cameras (EPIC); pn (Strüder et al. 2001), MOS1/2 (Turner et al. 2001), and the Optical Monitor (OM; Mason et al. 2001). Given the relatively low S/N of the EPIC data, we do not analyse the Reflection Grating Spectrometer (RGS) event data. The observation data files and the Pipeline Processing System products (PPS) were retrieved from the XMM-Newton Science Archive<sup>5</sup>. The EPIC data were reduced using v21.0.0 of the Science Analysis Software (SAS) designed for reduction of XMM data (Gabriel et al. 2004). We performed a filtering of event files using the SAS routine `evselect` and defined Good Time Intervals (GTI) to remove contamination from high flaring background times, with thresholds on the total CCD count rate defined via visual inspection of the light curve to be 0.5, 0.15 and 0.1 counts/s for pn, MOS1 and MOS2, respectively. This procedure resulted in total effective exposure times of 53.1, 65.1, and 67.3 ks for pn, MOS1 and MOS2, respectively. We extracted spectra for the source and adjacent background region in each camera, with apertures of radius 20 and 80 arcsec, respectively. We find the source is confidently detected in the 0.5–2.0 keV band in all three EPIC cameras, with PN, M1, and M2 yielding detection significances of  $9.3\sigma$ ,  $5.7\sigma$ , and  $7.3\sigma$ , respectively. These detections are consistent with the expectation from the re-analysis of the Chandra data. Aided by the significantly larger effective area at low energies ( $< 1.0$  keV), the source is also detected in the 0.2–0.5 keV band in PN ( $10.4\sigma$ ) and M2 ( $8.7\sigma$ ), although M1 alone does not yield a significant detection ( $2.3\sigma$ ). This further confirms the soft nature of the measured X-ray spectrum. The source counts, associated 90% confidence limits on source count rates, and detection significances are presented in the Appendix Table B.1. We also analyse the time-series EPIC data to search for periodicity in the X-ray emission<sup>6</sup>. The analysis of the X-ray spectra and light curves is presented in Sections 3.7 and 3.8.

The XMM observations also included exposures with the optical monitor in Fast Mode, using the UVW1 and UVM2 filters. The eight exposures with UVW1 had exposure times ranging from 2.5–4.4 ks, with a collective total of 32.9 ks. The eight exposures with UVM2 had exposure times of 4.4 ks with a collective total of 35.3 ks. For the analysis of the optical monitor data,

<sup>5</sup> <https://www.cosmos.esa.int/web/xmm-newton/xsa>

<sup>6</sup> We note that the time scale in the header after barycentric correction is rightly indicated as TDB (barycentric dynamical time); however, the comment to the entry remains unchanged (“XMM time will be TT (Terrestrial Time)”) and might generate confusion.

<sup>4</sup> <https://cxc.harvard.edu/cda/>

we make use of the time-series data provided in the pipeline data products of the pipeline processing system (PPS). Analysis of the simultaneous X-ray/UV/optical time-series data is presented in Section 3.8.

### 3. Analysis

#### 3.1. Periodicity analysis

Using the *astropy* implementation of the Lomb-Scargle periodogram, we derive a period of  $416.2431 \pm 0.0008$  s from the ZTF light curve in the *g* band. Using the three CHIMERA nights, we refine this estimate and look for a possible spin variation using the O-C (observed minus calculated) diagram. The O-C diagram shows the variation in phase of different observations (in the same filter) over long periods of time; such shifts could be introduced by an error on the estimated period or by a period derivative. If we define  $T_0$  as the time at which a minimum in the light curve occurs in the first observation, and  $P_0$  as our estimate of the period at the time  $T_0$ , for a small and constant period derivative ( $\dot{P} \ll P$ ), the shift in the time of arrival of the minimum in the light curve after a number of cycles  $n$  can be expressed as:

$$O - C = T_n - (T_0 + nP_0) \approx n\delta P + \dot{P}(P_0 + \delta P)\frac{n^2}{2} \quad (1)$$

where  $T_n$  is the time of the minimum at the cycle  $n$ ,  $\delta P$  is our error in the estimate of  $P_0$ , and  $\dot{P}$  is the period derivative, assumed constant.  $T_0 + nP_0$  is the expected ("calculated") time for the minimum at cycle  $n$ , while  $T_n$  is the observed time. A linear variation as a function of  $n$  indicates an error on the period, while a quadratic variation indicates the presence of a significant  $\dot{P}$ . From our three CHIMERA observations, we see no significant quadratic variation, and we can derive a  $3\text{-}\sigma$  limit on the period variation to be  $|\dot{P}| < 10^{-13}$  s/s. We can also refine our estimate of the spin period to  $416.243058 \pm 0.000008$  s.

#### 3.2. Magnetic models

The strongly shifted Lyman components observed in the COS spectrum indicate the presence of a high magnetic field strength ( $\approx 700$  MG) on the surface of ZTF J1901 and a hydrogen-dominated composition, confirming the previous estimates by C21. In the same paper, however, the characterisation of the physical properties of the WD (especially radius and effective temperature) hinged on modelling its SED with non-magnetic synthetic atmospheres. Since strong fields can dramatically alter the SED of a WD, we here aim to better constrain the properties of the star by using magnetic models instead.

We have developed state-of-the-art atmosphere models that include comprehensive opacity sets (e.g., Lamb & Sutherland 1974; Jordan 1992; Merani et al. 1995; Schimeczek & Wunner 2014) under a variable magnetic field strength. The models are in hydrostatic equilibrium and in joint radiative and convective equilibria. The line opacities include forbidden transitions enforced by a strong electric field (Zhao & Liu 2021; Liu & Zhao 2022), particularly the  $1s0 \rightarrow 2s0$  and  $1s0 \rightarrow 3d-2$  transitions identified in the FUV spectra of high-field magnetic WDs. In our models, for a given magnetic field geometry – dipole, quadrupole, multi-pole expansion, etc., viewed from any angle (Martin & Wickramasinghe 1979, 1981, 1984; Achilleos & Wickramasinghe 1989) – the visible hemisphere is discretised into 900 individual surface elements characterised by a local field strength and an angle between the field direction and the

line-of-sight. The temperature and density structures are computed for each surface element along with the angle-dependent intensity spectrum. These individual spectral elements are then co-added in spherical geometry to form the total emerging spectrum from the star. It is therefore possible to model the observed time- and an angle-dependent magnetic WD spectrum for each face of the WD.

In Fig. 5, we show several models for the same effective temperature ( $T_{\text{eff}} = 28,000$  K) and same magnetic field geometry on the surface of the WD (a dipole with inclination with respect to the line of sight of  $80^\circ$ ), at different magnetic field strengths at the pole (from  $B_p = 600$  to  $1,100$  MG). The dashed blue line shows a zero-field model for comparison. We can see that the magnetic field strongly affects the shape of the continuum, especially in the UV, redistributing the flux at different wavelengths, and that the effect is stronger for higher fields. Also, the shape and location of the absorption lines are determined by the magnetic field strength and structure over the surface. The location and shape of the broad absorption features in the  $2,000\text{--}3,000$  Å range, which are due to Balmer bound-free transitions, are also strongly dependent on the magnetic field strength and structure over the surface.

These new models include, for the first time, the effect on atmospheric structures of variable monochromatic opacities under a strong magnetic field. So far this effect had been neglected in the analysis of both low-field, say  $\lesssim 100$  MG (e.g., Külebi et al. 2009; Kepler et al. 2013; Hardy et al. 2023), and high-field magnetic WDs such as RE J0317–853/EUVE J0317–85.5 (e.g., Ferrario et al. 1997a; Burleigh et al. 1999; Vennes et al. 2003; Külebi et al. 2010). Although this simplifying assumption may hold true for low-field WDs, it breaks down at increasingly high fields (see Fig. 5). The new models will improve the analysis of the high-field, high-temperature ( $\gtrsim 25,000$  K) WDs in the samples of Külebi et al. (2009), Kepler et al. (2013) and Hardy et al. (2023). Improved models should eventually include exact bound-free opacities (Zhao 2021) superseding the present approximate opacities (see, e.g., Lamb & Sutherland 1974).

If a WD rotates, time-series observations, like the phase-resolved spectroscopy that we present in this paper for J1901, can reveal the variation of the field strength and structure on the surface of the WD, as each spectrum reveals the contribution of a different region via the variation in wavelength of the absorption lines and the modulation of the shape of the SED with the rotation period.

The exquisite HST dataset for J1901, combined with optical phase-resolved spectroscopy already presented in C21, can provide enough information to constrain the structure of the magnetic field over the surface of the WD. A proper modelling of these datasets, however, requires the development of an extensive suite of magnetic models with different geometries, at different magnetic field strengths and effective temperatures, and it is beyond the scope of this paper. In the next section, we employ a simple dipole structure to model the SED of the WD and constrain its physical properties. In an upcoming paper, we plan to develop a suite of magnetic models with different geometries to properly model the structure of the field on the WD.

#### 3.3. Modelling the spectral energy distribution of the WD

In Fig. 6, we show the SED of the WD, combining the phase-averaged spectrum from COS and STIS in the UV, with Pan-STARRS PS-1 photometry in the optical. We employ Pan-STARRS photometry and not the available LRIS optical spec-



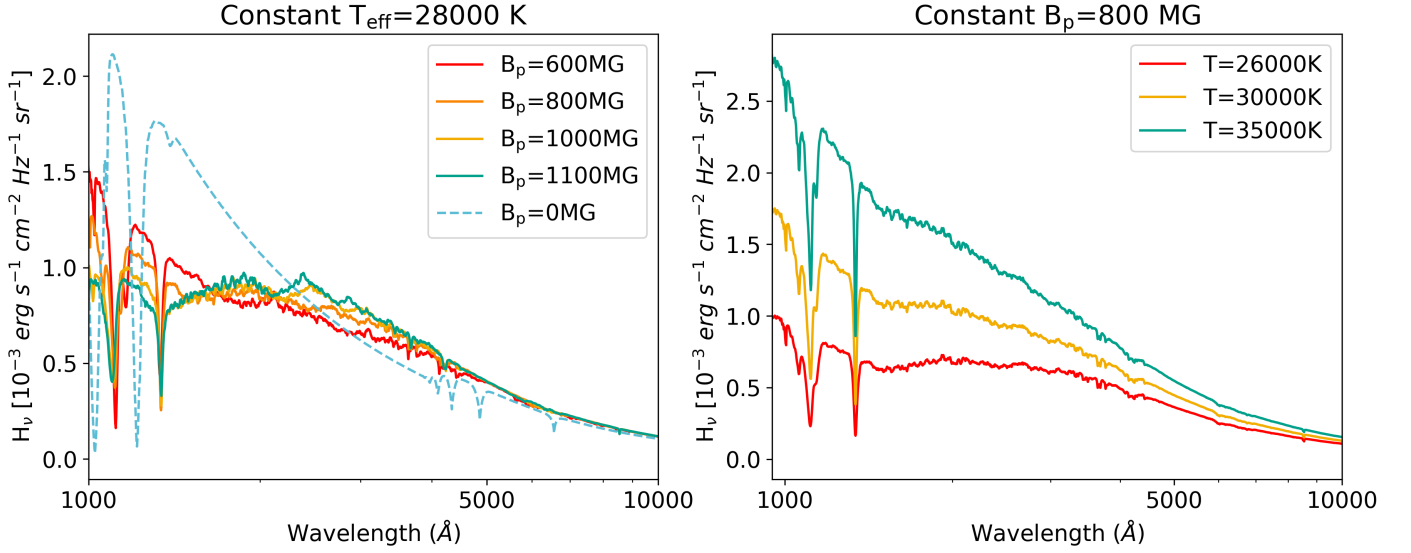


Fig. 5: **Left:** Our synthetic spectral models with the same effective temperature ( $T_{\text{eff}} = 28,000$ ) and magnetic field structure (a centred dipole with an inclination of  $80^\circ$  with respect to the line of sight) and different magnetic field strength at the pole (solid lines). Also, a zero-field model (Tremblay et al. 2013) is shown for comparison (dashed line). **Right:** Our spectral models for different  $T_{\text{eff}}$  for a constant dipole magnetic field of 800 MG.

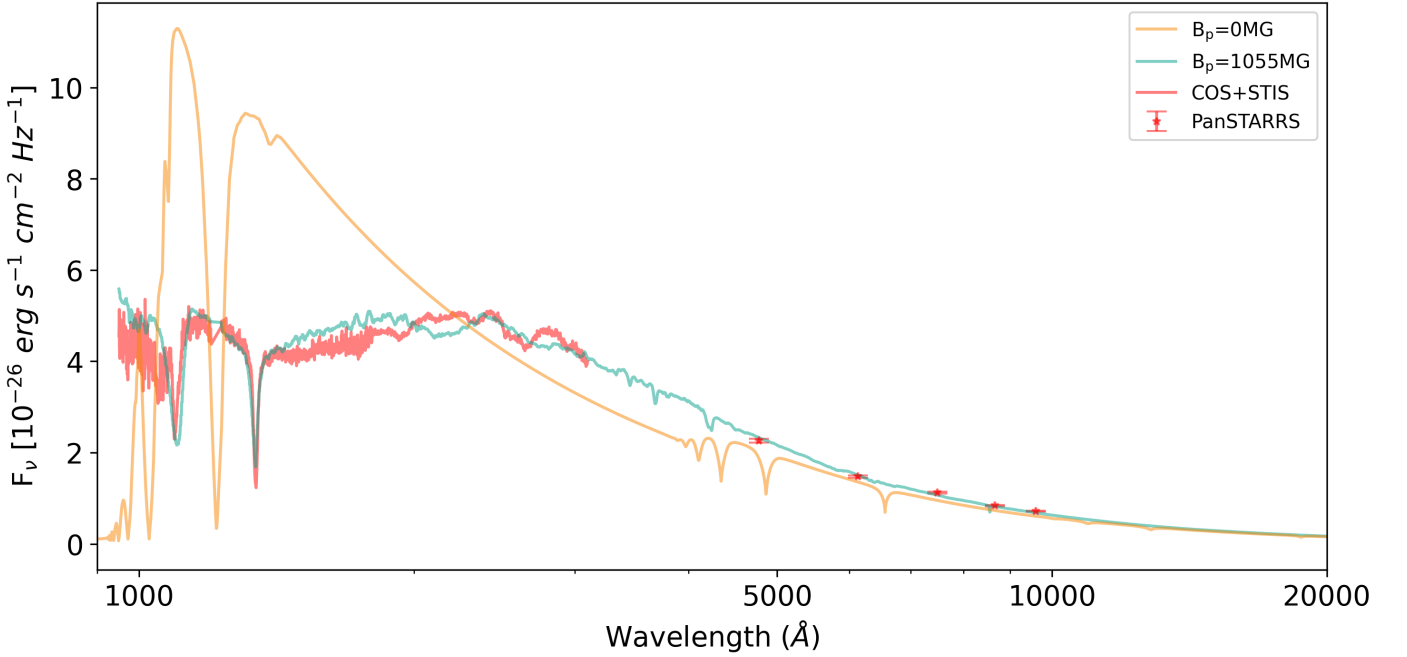


Fig. 6: Spectral energy distribution of J1901. The red line shows the phase-averaged spectrum from COS and STIS. The red points show the Pan-STARRS PS-1 photometry in the optical and near-infrared. The cyan line shows our best-fitting magnetic model, while the orange line shows a non-magnetic model with the same radius and temperature parameters for comparison.

troscopy because the flux calibration of the LRIS data is not accurate enough for our purposes. We can see that the SED shows a remarkable break at  $\sim 3,000\text{\AA}$ , where the steep optical spectrum flattens towards the UV. This behaviour has already been observed in other magnetic WDs with field strengths in excess of a few hundreds of MG (Green & Liebert 1981; Schmidt et al. 1986; Gänsicke et al. 2001; Cristea et al. 2025), but was until now unexplained, with absorption from cyclotron or metals invoked as possible causes. As we showed in the previous section (Fig. 5), this break is due to the effect of the magnetic field on

the opacities in the atmosphere of the WDs. In Fig. 6, we show that our model (solid cyan line), which includes the effects of the strong field on the monochromatic opacities and the temperature structure of the atmosphere, naturally reproduces the overall shape of the WD's SED.

We employ a grid of models with a fixed field geometry (a dipole with inclination with respect to the line of sight of  $80^\circ$ ), but with different field strengths and effective temperatures, to fit the SED of the WD. We use a simple Monte Carlo approach, implemented with emcee (Foreman-Mackey et al. 2013), and we

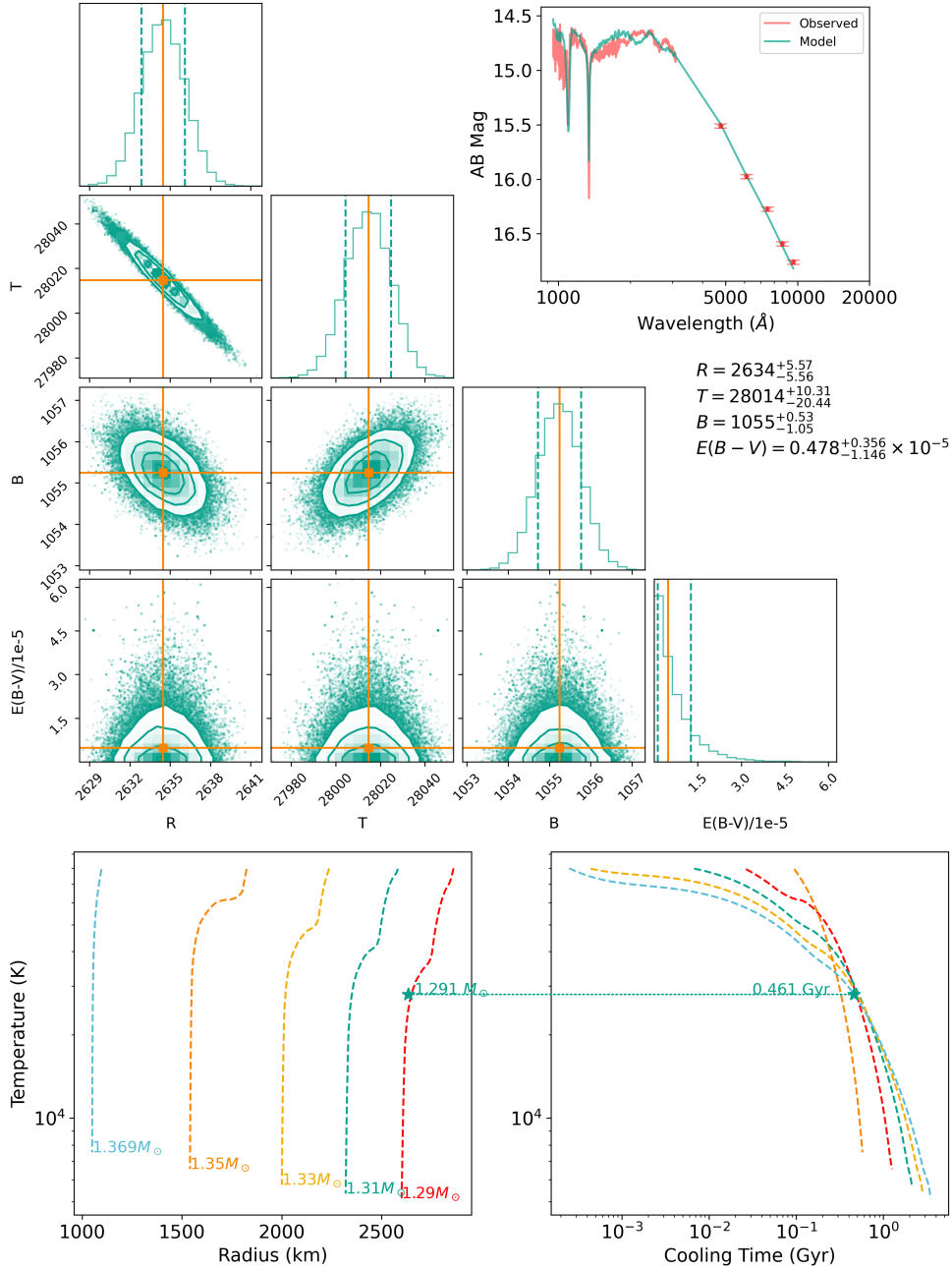


Fig. 7: **Top:** Corner plot with the marginalised distributions of the Radius, Temperature, Magnetic field and Extinction. The contours indicate the 1 and 3 sigma limits. **Bottom:** ONe-core WD evolutionary tracks for different masses from Althaus et al. (2023) (radius and cooling time vs. temperature). The star indicates the position of J1901 relative to the evolutionary tracks.

leave as free parameters: the effective temperature  $T_{\text{eff}}$ , the ratio between the radius of the WD and its distance from Earth  $R/D$ , the dipolar field strength of the WD,  $B_{\text{avg}}$ , and the extinction  $E(B-V)$  toward the WD. We account for extinction by reddening the synthetic models with the extinction curve from Gordon et al. (2023) in astropy. We derive the radius from the ratio  $R/D$  by employing the photogeometric distance estimate ( $D = 41.39 \pm 0.06$  pc, from Bailer-Jones et al. 2021).

Fig. 7 shows the corner plot of the marginalised distributions of the radius, effective temperature, magnetic field strength and extinction. The contours indicate the 1 and 3 sigma limits on the fitted parameters. The best-fit model is shown in Fig. 6 and the best-fit parameters are summarised in Table 2. The revised radius of  $\approx 2600$  km marks an increase from the earlier estimate

of  $\approx 2100$  km, placing the WD’s size closer to that of Titan – Saturn’s largest moon – than our own Moon.

As we can see in Fig. 6, our best-fitting model likely captures the representative average field strength on the WD surface, as the shape of the SED and the location of the two main Lyman absorption features are well represented. However, we can see that the geometry of the field that we chose for the model is likely different from the true field structure on the WD, as the shapes of the Lyman lines and of the Balmer edges in the 2000–3000 Å range are not well reproduced. As we mentioned in the previous section, modelling the correct structure of the magnetic field on the surface of the WD is beyond the scope of this paper; however, we caution the reader that the stellar parameters listed in Table 2 quote only statistical errors and we expect larger sys-

Table 2: Parameters of J1901

	ZTFJ1901
Gaia ID (DR2)	4506869128279648512
RA (ICRS)	285.386°
DEC (ICRS)	14.968°
Parallax (mas)	24.13 ± 0.05
T <sub>eff</sub> (K)	28,015 ± 20
Radius (Km)	2630 ± 10
Mass (M <sub>⊙</sub> )	1.31 ± 0.01 [CO], 1.29 ± 0.01 [ONe]
t <sub>cool</sub> (Gyr)	0.485 ± 0.01 [CO], 0.461 ± 0.01 [ONe]
B <sub>avg</sub> (MG)	721 ± 5
B <sub>p</sub> (MG)	1,055 ± 5
Period (s)	416.243058 ± 0.000008
E(B-V)	0
Reference Ephemeris <sup>a</sup> (MJD)	58753.38359598

<sup>a</sup> Reference ephemeris used to phase fold all lightcurves in this work. While  $B_p$  is the strength of the field at the magnetic pole,  $B_{avg}$  is the average magnetic field over the surface of the WD. We note that the uncertainties presented here are of purely statistical nature and do not yet take into account the systematic errors owing to the simplified modelling of the magnetic field.

tematic errors to be introduced by the simplified modelling of the magnetic field structure.

As can be seen in the marginalised distributions of the parameter posteriors in Fig. 7, the radius, temperature and magnetic field are clearly correlated. Since we only fit the average spectrum, this degeneracy is expected. The use of magnetic models and the extended UV coverage obtained thanks to HST provides, nonetheless, a significant improvement in the characterisation of the physical parameters of the WD compared to previous estimates. In an upcoming paper, we plan to develop a more sophisticated model that includes complex phase-dependent magnetic field geometry, which will allow us to break the degeneracy between the radius, temperature and magnetic field.

### 3.4. Inferring Mass and Cooling age

To infer the mass and cooling age of J1901, we employed the evolutionary cooling tracks of ultra-massive WDs presented by Althaus et al. (2022, 2023) for oxygen-neon (ONe) and carbon-oxygen (CO) core composition, respectively. These models provide the radius and effective temperature as a function of the cooling age of the WD for different WD masses, and incorporate detailed physics, including gravitational contraction, crystallisation, and relativistic corrections. WDs with masses above 1.1 M<sub>⊙</sub> that are the product of single-star evolution are expected to be composed mostly of oxygen and neon, with traces of carbon, sodium and magnesium, because the core in the progenitor star undergoes carbon burning before becoming a WD (Rakavy et al. 1967; Murai et al. 1968; García-Berro et al. 1997; Siess 2010; Kippenhahn et al. 2013), although the exact limit might depend on the progenitor star’s rotation (Dominguez et al. 1996) and on

stellar winds (Althaus et al. 2021). Even in the case of merger remnants, compressional heating during the merger is expected to ignite off-centre carbon burning (Shen et al. 2012), resulting in an ONe WD (Schwab 2021b). However, whether or not the carbon-ignition mass is different in WD mergers, and if some ultramassive merger remnants might have CO cores, is still under debate (Wu et al. 2022; Shen et al. 2023; Sousa et al. 2023; Blatman & Ginzburg 2024). We therefore employ both models and present both mass estimates. As we derive extremely high masses, the core composition is likely ONe, no matter the evolutionary history of the WD.

Given the radius and effective temperature obtained from our SED fitting, we constructed a two-dimensional interpolator of radius in the mass–temperature plane. We then employed Brent’s root-finding algorithm (Brent 1973) to determine the mass corresponding to our observed radius at the fixed effective temperature. Brent’s method is ideal for this problem because it robustly identifies unique solutions within bounded intervals, respecting the monotonic relationship between mass and radius at fixed temperature. Subsequently, the inferred mass allowed us to interpolate directly from the models to estimate the cooling age of the WD. We list our best estimates for the ONe and CO compositions in Table 2. We note that the inferred cooling age of  $\approx 480$  Myr makes it remarkably older than the earlier estimate for its age between 10–100 Myr, which becomes important when constraining the formation rate of such systems, which is beyond the scope of this work. We note that the estimates for mass and cooling age are obtained from evolutionary models of ultra-massive WDs that account for relativistic effects (see Althaus et al. 2022, 2023). The Newtonian models, for example, predict a cooling age of  $\approx 500$  Myr for the same radius and temperature.

### 3.5. Lack of a companion

As we explain in more detail below, the observed X-ray emission is too hard and too bright to be due to the photospheric emission of the hot WD. One possible explanation is the interaction of the WD with infalling circumstellar material. We analyse the possibility that this material is supplied by a stellar or substellar companion as the donor in a binary system.

As can be seen in the lower left panel of Fig. 8, the near-infrared flux, at 1–2.5  $\mu\text{m}$ , is consistent with the WD’s continuum alone: the best-fitting magnetic model (cyan line), that we fitted only on the optical and UV data, goes through the UKIDSS photometry without showing any excess. Because the WD is very hot, a brown dwarf close enough to fill its Roche lobe would be irradiated. We can calculate the irradiation temperature for the brown dwarf with

$$T_{\text{irr,BD}} \approx T_{\text{eff,WD}} \sqrt{\frac{R_{\text{WD}}}{2a}} \sqrt[4]{(1 - A_B)}, \quad (2)$$

where  $A_B$  is the Bond albedo (Jermyn et al. 2017; Lothringer & Casewell 2020) for the brown dwarf,  $R_{\text{WD}}$  and  $T_{\text{eff,WD}}$  are the WD radius and effective temperature, and  $a$  is the orbital separation. The effective temperature of the brown dwarf would be the effective sum of the fluxes:

$$T_{\text{tot,BD}} = \sqrt[4]{T_{\text{irr,BD}}^4 + T_{\text{int,BD}}^4}, \quad (3)$$

where  $T_{\text{int,BD}}$  is the temperature that an isolated brown dwarf would display at its current evolutionary state. To estimate the brightness that we would expect from a Roche lobe filling brown dwarf companion, we calculate the irradiation temperature for



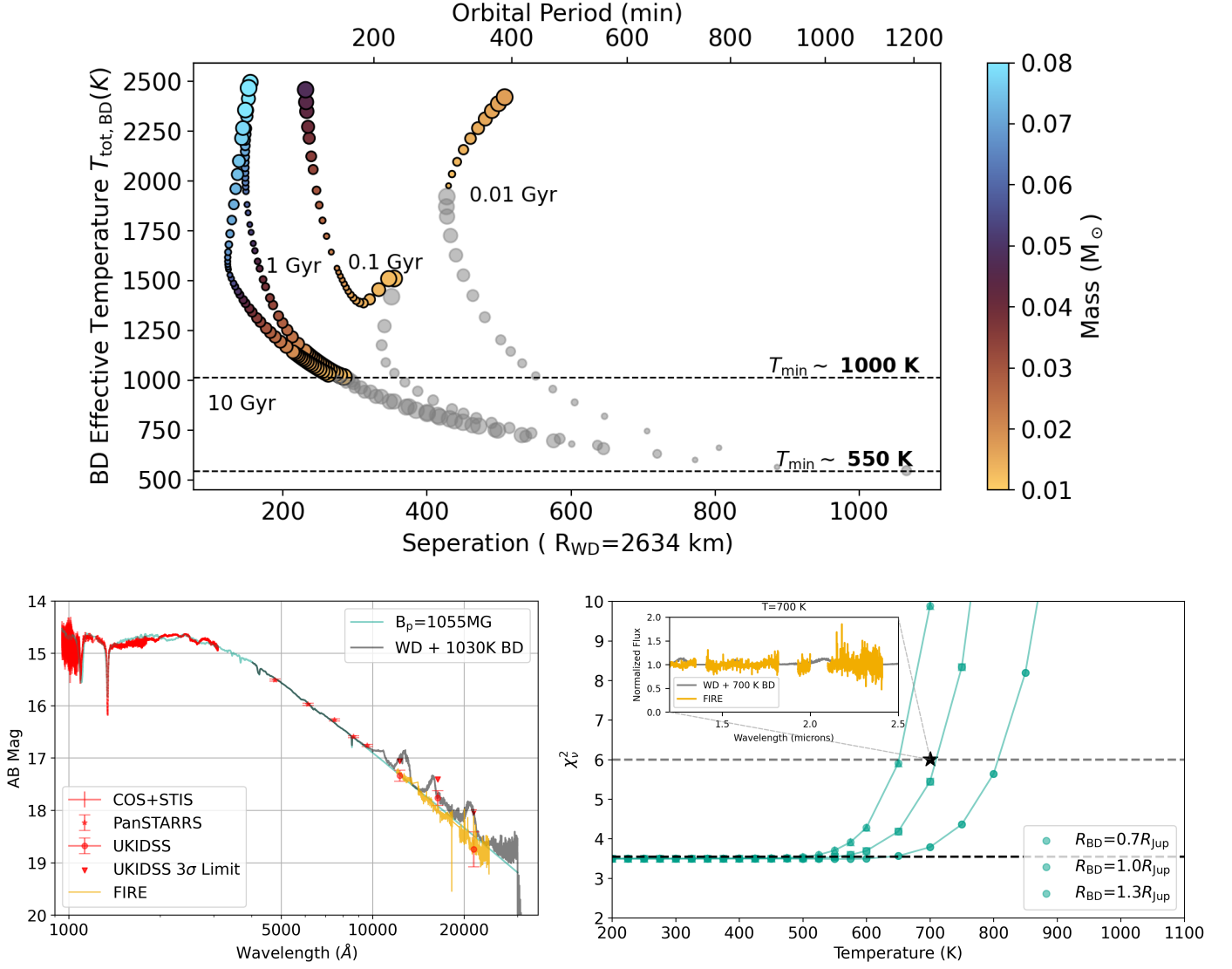


**Fig. 8: Top:** BD effective temperature  $T_{\text{tot, BD}}$  (Eq. (3)) of a Roche-lobe-filling brown dwarf companion as a function of orbital separation (bottom axis, in units of the WD’s radius,  $R_{\text{WD}} \approx 2646$  km) and corresponding orbital period (top axis). Coloured points denote different companion masses (colour bar in  $M_{\odot}$ ). The grey points are companions with  $M \leq 0.01 M_{\odot}$ . The size of the scatter points corresponds to the radii of the corresponding brown dwarfs. The ages are mentioned beside the corresponding tracks. **Bottom Left:** Combined spectral energy distribution (SED) of ZTF J1901, spanning far-UV to near-IR. Red symbols show HST/COS+STIS spectroscopy (far-UV; smoothed red curve) and photometry from Pan-STARRS (optical) and UKIDSS (near-IR). The yellow spectrum in the IR is the smoothed spectrum obtained from FIRE. The cyan curve shows the modelled magnetic WD atmosphere, which closely fits the data from 1–2.5  $\mu\text{m}$ . A hypothetical brown dwarf companion’s contribution (grey curve) is included for illustration. **Bottom Right:** Reduced  $\chi^2_{\nu}$  metric as a function of brown dwarf temperature. The different markers correspond to the tracks of constant  $R_{\text{BD}}$  for a fixed  $\log(g) = 4$ .

brown dwarfs at different masses. We employ the brown dwarf evolutionary and spectral models of Marley et al. (2021). More massive brown dwarfs have to orbit at smaller separations to fill their Roche lobes, and thus they would intercept a larger fraction of the WD’s luminosity. For example, a  $0.05 M_{\odot}$  brown dwarf at 1 Gyr would fill its Roche lobe at  $\approx 170 R_{\text{WD}}$  separation (orbital period  $P \sim 1.1$  h) and attain  $T_{\text{irr, BD}} \sim 2000$  K using Eq. (2). In contrast, a  $0.01 M_{\odot}$  at 1 Gyr dwarf must orbit further out ( $\sim 1 R_{\odot}$ ,  $P \sim 2.7$  h) to fill its Roche lobe and would be heated to only to  $T_{\text{irr}} \sim 1000$  K. In the calculation, we assume conservatively a moderately high albedo ( $A_B = 0.5$ , brown dwarfs are expected to have lower albedo, Marley et al. 1999; Hernández Santiste-

ban et al. 2016) and full heat redistribution, so that  $T_{\text{irr}}$  represents the roughly uniform day-side surface temperature. The upper panel of Fig. 8 shows the total temperature of the brown dwarf as a function of its Roche lobe filling distances, in units of the WD radius. The upper x-axis shows that, as the orbital period increases (separation widens), the irradiation temperature drops markedly. The different tracks show distinct model ages, the marker sizes are proportional to the radii and the colourbar shows the brown dwarf masses. Models corresponding to the planetary regime ( $< 13 M_{\text{Jup}}$ ) are shown in grey. It can be seen that the minimum brown dwarf irradiation temperature attainable is  $T_{\text{tot, BD}} \approx 1000$  K for a 1-10 Gyr brown dwarf. We also

mark the lowest mass planet in the Sonora grid ( $\approx 0.5 M_{\text{Jup}}$ ), which would fill its Roche lobe at a period of  $\approx 1100$  minutes with a temperature of  $\approx 550$  K.

The near-IR non-detections allow us to rule out a wide range of companion scenarios that would otherwise produce detectable excess emission. The bottom-left plot in Fig. 8 shows the observed WD SED from the UV to the infrared (in red) compared to the best-fitting magnetic WD model (in cyan). For the infrared, we show the UKIDSS photometry (in red circles) and the FIRE spectrum (yellow solid line) normalised to the UKIDSS J-band value (the poor flux calibration in the FIRE spectroscopy does not allow us to obtain a reliable absolute flux). The UKIDSS photometry alone allows us to exclude any brown dwarf companion with a temperature higher than 1000 K, excluding all possible Roche-lobe-filling brown dwarf companions.

The FIRE spectrum allows us to exclude even colder objects. We cannot use the FIRE spectrum directly to constrain the contribution of a possible companion to the total flux in the infrared due to known flux calibration issues with the FIRE spectrograph (see Simcoe et al. 2008; Sullivan & Simcoe 2012). For example, Vito et al. (2021) reports that the normalisation of their spectrum from FIRE is  $\approx 15\%$  lower than previously recorded spectra for the same object, attributing the difference to varying seeing conditions. However, the spectrum of a cool brown dwarf presents strong molecular absorption features, and we can use the lack of detected absorption features in the smooth FIRE spectrum to put an even more stringent constraint on the temperature of a possible companion. To do so, we compare the observed FIRE spectrum to a model spectrum that combines the best-fitting magnetic WD atmosphere model with a brown dwarf model of a certain temperature, and see at what brown dwarf temperature we would expect to see absorption features in the FIRE spectrum. For the brown dwarf contribution, we utilise the spectral models provided by Marley et al. (2021). Because we cannot trust the absolute flux calibration in the FIRE spectrum, we normalise both the observed and the model spectra. For the FIRE spectrum, we compute the normalised flux by fitting the spectrum with a 4-order polynomial. The combined model flux is normalised using the WD continuum. We then compute the reduced chi-squared,  $\chi^2_{\nu}$ :

$$\chi^2_{\nu} = \frac{1}{N-1} \sum_{i=1}^N \left( \frac{F_{\text{obs},i} - F_{\text{model},i}}{\sigma_{\text{obs}}} \right)^2. \quad (4)$$

where  $F_{\text{obs}}$  and  $\sigma_{\text{obs}}$  represent the normalised observed flux and its associated error, respectively, while  $F_{\text{model},i}$  denotes the normalised total model flux ( $F_{\text{BD}} + F_{\text{WD}}$ ). Using Eq. (4), we calculate  $\chi^2_{\nu}$  for various brown dwarf temperatures, and we show our results in the bottom right panel of Fig. 8. For each model, we assumed a constant  $\log g$  and varied radius between 0.7 and 1.3  $R_{\text{Jup}}$ , which are the expected bounds on the radius of a brown dwarf through its evolution. The lowest temperature normalised models are indistinguishable, within the errors of the spectrum, from a flat line at 1, and their fit should yield a reduced  $\chi^2_{\nu}$  close to unity. However, since the issues in the FIRE spectrum flux calibration introduce correlated noise that is larger than the estimated uncertainties, we find a  $\chi^2_{\nu} \approx 3.5$  across the coolest models. As the temperature increases beyond this regime,  $\chi^2_{\nu}$  remains near  $\approx 3.5$  at low T, then rises sharply at higher temperatures. At low brown dwarf temperatures, the brown dwarf absorption features are too small to be detected at the signal-to-noise level of the FIRE spectrum, so the  $\chi^2_{\nu}$  is not affected by the change in

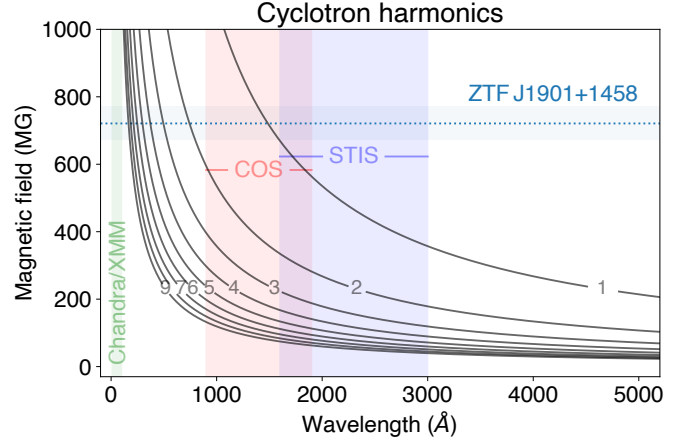


Fig. 9: Central wavelength of the first nine cyclotron harmonics for mean surface magnetic field strengths. For the inferred magnetic field strength of ZTF J1901 ( $B_{\text{avg}} \approx 720$  MG), all harmonics are predicted to fall in the UV and EUV.

temperatures. As we go to higher temperatures, the strong features in the spectrum make the model deviate from the observed spectrum and increase the  $\chi^2_{\nu}$ . The sharp rise in  $\chi^2_{\nu}$  shows that our spectrum excludes brown dwarfs with temperatures exceeding approximately 700 K (shown in the inset).

### 3.6. Cyclotron harmonics and expected signatures

Cyclotron emission arises from charged particles—typically electrons—spiralling in magnetic fields, producing a characteristic set of harmonics at multiples of the cyclotron fundamental frequency. In highly magnetised WDs, these features can appear as discrete humps in optical or UV spectra, depending on the field strength and viewing geometry. The energy of the fundamental cyclotron photon in a magnetic field  $B$  is:

$$E_{\text{cyc}} = \frac{\hbar e B}{m_e c} \approx 11.6 \text{ eV} \left( \frac{B}{10^9 \text{ G}} \right), \quad (5)$$

corresponding to a wavelength

$$\lambda_{\text{cyc}} = \frac{hc}{E_{\text{cyc}}} \approx 1100 \text{ Å} \left( \frac{10^9 \text{ G}}{B} \right). \quad (6)$$

Figure 9 plots the central wavelengths of the first nine harmonics for  $B_{\text{avg}} = 7 \times 10^8$  G. We see that, except for the first harmonic, which overlaps with our COS spectrum, all the other harmonics lie in the EUV. In our UV spectrum, we see no discrete cyclotron harmonic feature consistent with the first harmonic. The lack of a cyclotron emission in the COS spectrum might indicate that there is very little (or no) active accretion onto the WD surface or that most of the power is in the higher harmonics, which are out of reach in the EUV.

### 3.7. Analysis of the X-ray spectrum

We perform an X-ray spectral analysis using the software package Bayesian X-ray Analysis (BXA; Buchner 2016) which connects ULTRANEST (Buchner 2016) – a nested sampling algorithm – with an X-ray spectral fitting environment. For the spectral fitting environment, we adopt XSPEC (Arnaud 1996) operated via

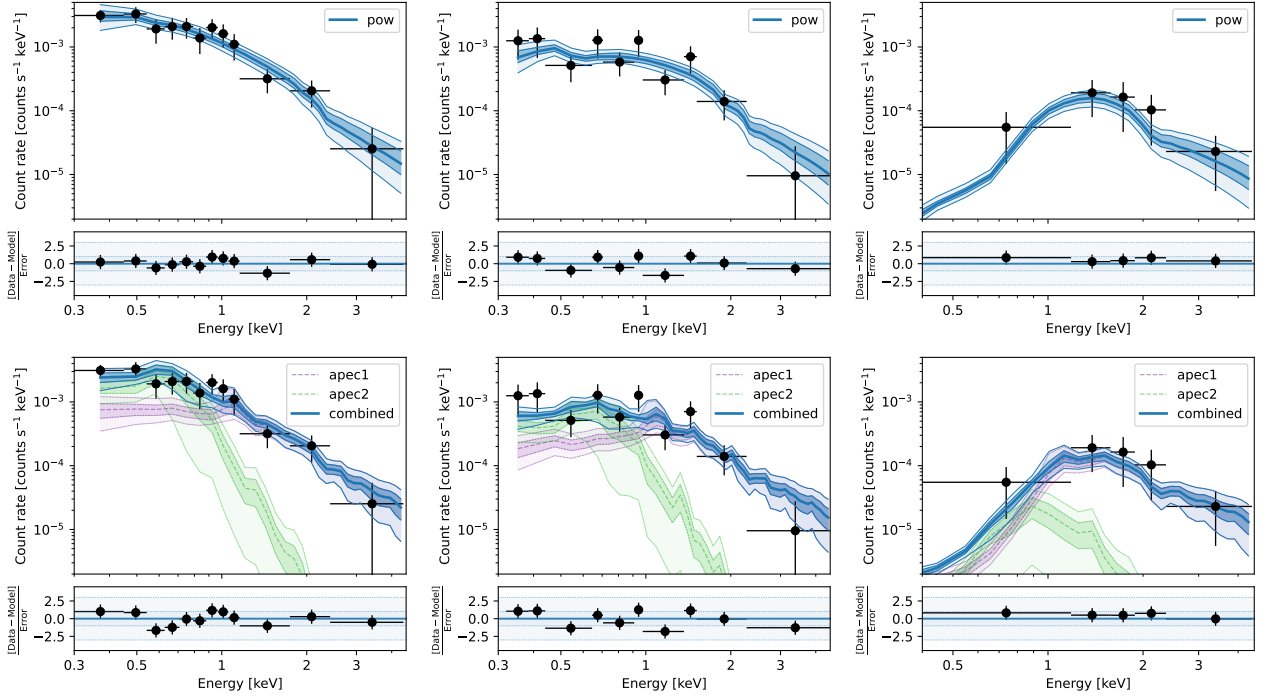


Fig. 10: Fit to the available archival X-ray spectroscopic data, including XMM EPIC PN (left) and MOS (middle) and Chandra ACIS-I (right). The top panels show a fit using an absorbed power law model, whilst the bottom panels employ a 2-temperature isothermal plasma model (APEC) with an absorption component. The data points show the binned X-ray spectra, whilst the best-fitting model fit is shown in blue. Contours indicate 1 and 3 sigma limits on the best-fitting model, including the two individual APEC components in the bottom panels.

its PYTHON interface, PYXSPEC. We perform a simultaneous fit of the background-subtracted Chandra ACIS-I and XMM-Newton EPIC PN and MOS data, using the Cash statistic, or C-statistic, necessary for the accurate fitting of data in the low-count regime (Cash 1979). Before fitting, the spectra were binned using the optimal binning algorithm of Kaastra & Bleeker (2016). We fit the data using two models, namely i) a simple power law and ii) a 2-temperature, optically-thin plasma model (APEC). For the second model, we adopt Solar abundances as presented by Asplund et al. (2009). In both models, we include an absorption component to account for the Galactic  $n_{\text{H}}$  absorption and intrinsic absorption at the system. With a distance of 41 pc, the system is sufficiently close to Earth that the Galactic  $n_{\text{H}}$  absorption should be minimal, and we thus adopt a uniform prior on the absorption. We impose a uniform prior on the photon index in the power law model and plasma temperatures in the 2-temperature optically-thin plasma model. For the normalisations in both models, we adopt log-uniform priors.

Fig. 10 shows the best-fitting models for the power law (top panels) and 2-temperature (APEC) models (lower panels). We show the PN, MOS (combined M1 & M2), and ACIS-I spectra in the left, middle and right panels, respectively. The thick line shows the best-fit model with the 1- and 3- $\sigma$  range of uncertainty indicated in the shaded regions. For the 2-temperature model, we also show the two individual components. The posterior distribution for the fitted parameters of the power law and APEC models can be found in the Appendix, Fig. B.1. For the power law model, we find a photon index of  $\Gamma = 2.9^{+0.4}_{-0.3}$ . For the 2-temperature plasma model, we find a soft component with temperature  $kT = 0.23 \pm 0.03$  keV, and a harder component with temperature  $kT = 2.95^{+1.23}_{-0.81}$  keV. We estimate the flux in the 0.25–10 keV band by integrating the best-fitting 2-

temperature APEC model across this energy range. We find a flux of  $F_{\text{X}}[0.25 - 10.0 \text{ keV}] = 6.58^{+0.93}_{-0.78} \times 10^{-15} \text{ erg s}^{-1} \text{ cm}^{-2}$ . At measured distance of  $D = 41$  pc, this yields an X-ray luminosity of  $L_{\text{X}}[0.25 - 10.0 \text{ keV}] = 1.28^{+0.18}_{-0.15} \times 10^{-15} \text{ erg s}^{-1}$ . If the X-rays were generated by material infalling from infinity to the surface of the WD, we can estimate a lower limit on the mass accretion rate by assuming that all the gravitational energy is converted into X-rays. The accretion rate can be thus estimated from the X-ray luminosity using the expression (Patterson & Raymond 1985):

$$\dot{M}_{\text{X}} = \frac{2}{A} L_{\text{X}} \frac{R_{\text{WD}}}{GM_{\text{WD}}} \approx 3.8 \times 10^9 \text{ g/s} \quad (7)$$

where for the mass and radius of the WD ( $M_{\text{WD}}$  and  $R_{\text{WD}}$ ) we have used the estimates from Sections 3.3 and 3.4, and the factor two accounts for 50% of the emitted photons being directed back towards and absorbed by the star. The constant  $A$  quantifies the fraction of the total accretion luminosity carried in the observed band, which we set to 1 (to obtain a lower limit).

We use Bayesian evidence to compare the two models used in the spectral analysis of the X-ray data. We make use of the model comparison framework within BXA (see Buchner et al. 2014), to evaluate the Bayesian evidence in support of the power law model ( $Z_{\text{pow}}$ ) and APEC ( $Z_{\text{apec}}$ ). The Bayes factor for the comparison of the two models is given by  $K = Z_{\text{pow}}/Z_{\text{apec}}$ , from which we find a value of  $K \approx 150$ . This provides strong evidence in favour of the power law model over the 2-temperature optically-thin plasma model with Solar composition. However, we point out that our analysis only compares these two specific models and does not indicate that a non-thermal model is preferred in absolute terms. Other thermal models, like a 3-



temperature model, a cooling flow model, or a model with a different composition of the optically thin plasma might fit the data better than the two models presented in this paper. We did not perform additional fits because the signal-to-noise in the spectra is likely not sufficient to discern between many different models; however, deeper observations could provide additional hints on the nature of the emission – in particular regarding the spectral properties in and out of the pulse (see Fig. 11; lower panel). We also check whether the relatively favoured model provides a reasonable fit to the data using the XSPEC *goodness* routine, which uses Monte Carlo simulations to estimate the fraction of synthetic datasets that would yield a better fit statistic than the observed data. From 1000 samples, we find that 66.90% of the simulated spectra have lower, or better, fit statistics compared to our best-fitting model, which implies that the model is a reasonable description of the observed data. We thus conclude that the power law model provides an adequate fit for the measured X-ray spectroscopic data.

### 3.8. X-ray variability

Extraction of a light curve with the SAS tools can be problematic in the low count rate, background-dominated regime because this procedure generally requires to bin event times. To investigate periodic X-ray variability, we instead phase-fold the barycentric-corrected event times onto a range of trial periods and search for evidence of periodicity by a  $\chi$ -squared rejection of a constant count rate. We present here this analysis for events with energies in the range 0.3–1.0 keV, and bin the counts into 5 phase bins for each trial period. This energy range is chosen to maximize the S/N. We find that our results are broadly insensitive to changes in the energy range and number of phase bins chosen. To the phase-folded light curve, we fit a line of constant count rate, and interpret the chi-squared value as a statistical rejection of constant flux. Under this procedure, large chi-squared values indicate periodic variability at the given trial period. Fig. 11 shows the results of this test on the source events measured during the observation by the EPIC PN camera. The top panel shows that the strongest period detected lies near that measured from optical photometry. The second strongest period in the top panel is a sub-harmonic, with a period of  $P = 2P_{\text{max}}$ . The middle panel shows that the period recovered in the X-ray analysis matches closely that recovered through optical photometry. The bottom most panel shows the phase-folded lightcurve. We repeated the analysis for both MOS cameras, but the lower source count rate yielded a less significant detection. The light curves in the UVW1 and UVM2 filters of the Optical Monitor showed no phase variation compared to those obtained from COS and STIS spectra in the same wavelength ranges.

## 4. Discussion

### 4.1. An extreme and isolated merger remnant

In the previous section, we have employed our new magnetic models and the new HST spectroscopy to derive stronger constraints on the physical parameters (temperature, radius, mass, cooling age and magnetic field strength) of J1901. The updated parameters, with the exception of the effective temperature, are broadly consistent with those reported in C21, and confirm the nature of the WD as an extremely massive, highly magnetised and rapidly rotating merger remnant. The slightly larger radius that we derive (by a few hundred kilometres) and correspondingly lower mass do not alter the basic picture: this star is one of

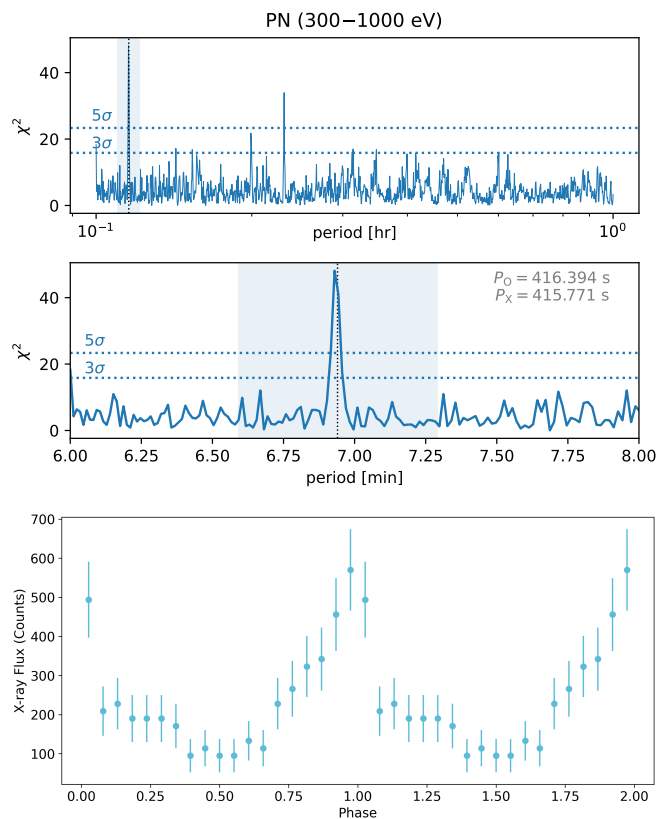


Fig. 11: **Top and Middle:** Chi-squared periodogram for the EPIC PN source events. The chi-squared value indicates the goodness-of-fit for a constant count rate after phase folding the event times at each of the periods shown. Large chi-squared values indicate periodic variability via the statistical rejection of a constant count rate. This procedure recovers the optical photometric period. Sigma detection thresholds are defined as multiples of the standard deviation of all measured chi-squared values. **Bottom:** Phase-folded lightcurve of the XMM data.

the most compact and massive merger remnants known. However, the new radius and mass estimate change the expected central density of the WD. Using the density profiles from Althaus et al. (2022, 2023), we find the central density of the WD to be  $7.55 \times 10^8 \text{ g cm}^{-3}$  and  $7.31 \times 10^8 \text{ g cm}^{-3}$  for the CO and ONe core compositions respectively. These estimates are close to but **below** the threshold for electron capture onto sodium ( $1.7 \times 10^9 \text{ g cm}^{-3}$ , Schwab et al. 2017). Moreover, Althaus et al. (2022) predict that an ONe core WD at this mass and temperature should already have crystallised  $\approx 50\%$  of its stellar mass ( $\approx 80\%$  in the case of a CO core). It is therefore unlikely that the star is undergoing Urca cooling at this moment, as previously suggested by C21 and Schwab (2021a). However, J1901 could still undergo important  $^{22}\text{Ne}$  distillation during crystallisation. As discussed by Salaris et al. (2024) and Salaris et al. (2024), the solid phase that forms within the core is relatively depleted in  $^{22}\text{Ne}$ , which remains in the surrounding liquid and can migrate inward under gravity. This process releases additional energy and can delay cooling substantially, potentially affecting the evolutionary timescales for a star with a large crystallised fraction like J1901. In the models, the central temperatures in the core, which are important to constrain axion production, are  $\approx 1.45 \times 10^7 \text{ K}$  for both the CO and ONe core compositions.

Table 3: X-ray properties of J1901 derived from BXA fit to the XMM and Chandra data as part of this study.

	J1901
Flux [ $10^{-15}$ erg s $^{-1}$ /cm $^2$ ] <sup>a</sup>	$6.58^{+0.93}_{-0.78}$
Luminosity [ $10^{27}$ erg s $^{-1}$ ]	$1.28^{+0.18}_{-0.15}$
$kT_1$ [keV] <sup>c</sup>	$2.95^{+1.23}_{-0.81}$ keV
$kT_2$ [keV] <sup>c</sup>	$0.23 \pm 0.03$
$\dot{M}_X$ [ $10^9$ g/s] <sup>b</sup>	$\approx 3.8$
$\dot{M}_X$ [ $10^{-17} M_\odot$ /yr] <sup>b</sup>	$\approx 6$

<sup>a</sup> The measured X-ray flux and all derived X-ray parameters correspond to the energy band 0.25–10.0 keV. The 68% and 90% confidence limits on these parameters, and those for a soft band (0.25–2.0 keV), can be found in the Appendix Tables B.1. <sup>b</sup> Accretion rates are computed assuming that approximately half of the gravitational potential energy is converted into X-ray luminosity (Patterson & Raymond 1985). <sup>c</sup> Parameters for the fit obtained using the two-temperature APEC model.

We note that, since we underestimate the errors on the effective temperature and radius, we are also underestimating the errors on the mass and cooling age. Since the central density is extremely dependent on the mass, any subsequent estimate for electron capture is open to revision. We intend to address this factor in a follow-up study on J1901.

From the infrared analysis, we also exclude the possibility of the WD being the accretor in a mass-transferring binary with a Roche-lobe-filling stellar or substellar companion. The coldest brown dwarf that would be consistent with the UKIDSS photometry and FIRE spectroscopy has a temperature below 700 K (see Fig 8); this is significantly below the lower limits on irradiation temperatures for any brown dwarf above  $13 M_{\text{jup}}$ . Each band in the UKIDSS photometry was obtained in different nights, and for the  $K_s$  band, we have two different observations taken in two separate nights, which do not show any hint of variability between the two epochs. Given the possible brown dwarf orbital periods, it is highly unlikely that we have only observed the cold, non-irradiated face of a potential brown dwarf in all instances (including the 1.5-hour-long FIRE spectroscopy). Hence, we confidently rule out the presence of a Roche-lobe-filling brown dwarf companion and, implicitly, that of accretion due to ongoing mass transfer as part of a cataclysmic variable evolution scenario. It is, however, still possible for a cold planet to be the mass donor in the system, given the orbital period at which it would be filling its Roche lobe. Another possibility, given the very small accretion rate, would be the presence of a somewhat more distant companion brown dwarf not filling its Roche lobe, but transferring material through a weak wind, although currently, direct evidence of winds has not been observed from any brown dwarf.

#### 4.2. Origin of the optical and UV variability

As we can see in Fig.s 1 and 2, the Lyman absorption features in the COS spectrum vary slightly in wavelength and shape over the rotation period, indicating a variation of the field strength over the surface of the WD. The continuum across the UV and the optical also varies in a non-trivial way with period, showing a sinusoidal variation that shifts in phase with wavelength. To study the variability in the UV, we extracted light curves from the HST

data in six ad hoc bands, three in the COS wavelength range (we call them C1, C2 and C3) and three in the STIS wavelength range (S1, S2 and S3, see Figure 1). The light curves, folded on the spin period of the WD, exhibit an approximately sinusoidal variation, with an increasing amplitude toward bluer wavelengths. As we can see in Fig.12, where we compare the UV light curves with the light curves from ZTF in  $g$ ,  $r$  and  $i$  and from LightSpeed in  $u$ , the amplitude increases monotonically from the red optical to the far UV, while the shift in phase does not follow a clear pattern.

This phase-dependent variability in the continuum is most naturally explained by the varying magnetic field on the surface of the WD (Ferrario et al. 1997b). As the WD rotates, regions with different magnetic field orientations and local strengths contribute to the emission. As a proof of concept, we take a set of our magnetic models with the same effective temperature (28,000 K) and magnetic field geometry (a dipole with inclination with respect to the line of sight of  $80^\circ$ ) but at different magnetic field strengths, between 600 and 900 MG (shown in Fig. 5), and we extract the flux in the observed bands ( $g$ ,  $r$  and  $i$  in the optical, and the 6 bands that we define as C1–S3 in the UV) for each model. The lower panels of Fig. 13 show the variation in flux in the different bands between the different models as a function of magnetic field strength (each marker is a different model, and we vary the magnetic field up and down between 600 and 900 MG twice). These curves are remarkably similar in amplitude to the observed light curves in the respective bands (shown in the upper panels); moreover, they display strong shifts in phase between different bands, similar to what is observed in the light curves, although not exactly of the same magnitude. In reality, we stress that the curves shown in the bottom panels do not represent a realistic model for our light curves, as we kept the geometry fixed and we just varied the magnetic field strength, while in a real rotating WD, we would have to rotate the field as well. However, this proof of concept shows that the observed variability can, in principle, be explained simply by the variation of field strength on the surface of the WD, without invoking additional effects such as temperature variations over the surface. A full, detailed phase-resolved analysis (including synthetic spectra calculations incorporating the Zeeman split components) is needed to refine these estimates. This will be the focus of a follow-up paper. Spots, temperature variations or composition inhomogeneities across the surface could also contribute to the observed variability. Together, these different mechanisms could combine to produce the complex phase and wavelength dependent variability seen in the data.

#### 4.3. Origin of the X-Ray Emission

Hot WDs ( $T_{\text{eff}} \geq 25,000$  K) can be detected in the X-rays because of their soft photospheric emission (see e.g. Jordan et al. 1994; Vennes 1999; O’Dwyer et al. 2003); however, the X-ray spectrum of J1901 is too hard and too bright to be consistent with photospheric emission: a  $T_{\text{eff}} \approx 28,000$  K hydrogen atmosphere peaks in the far-UV and would produce a negligible flux above  $\approx 0.1$  keV. The observed X-rays must therefore be powered by a different mechanism, most likely by the interaction of the WD or its magnetosphere with circumstellar material. We have demonstrated that the WD is not part of a mass-transferring binary, as we have excluded all possible Roche-lobe-filling stellar or brown dwarf companions (see Section 3.5), and we currently do not have strong observational constraints on the origin of the circumstellar material, but we can advance some hypotheses.

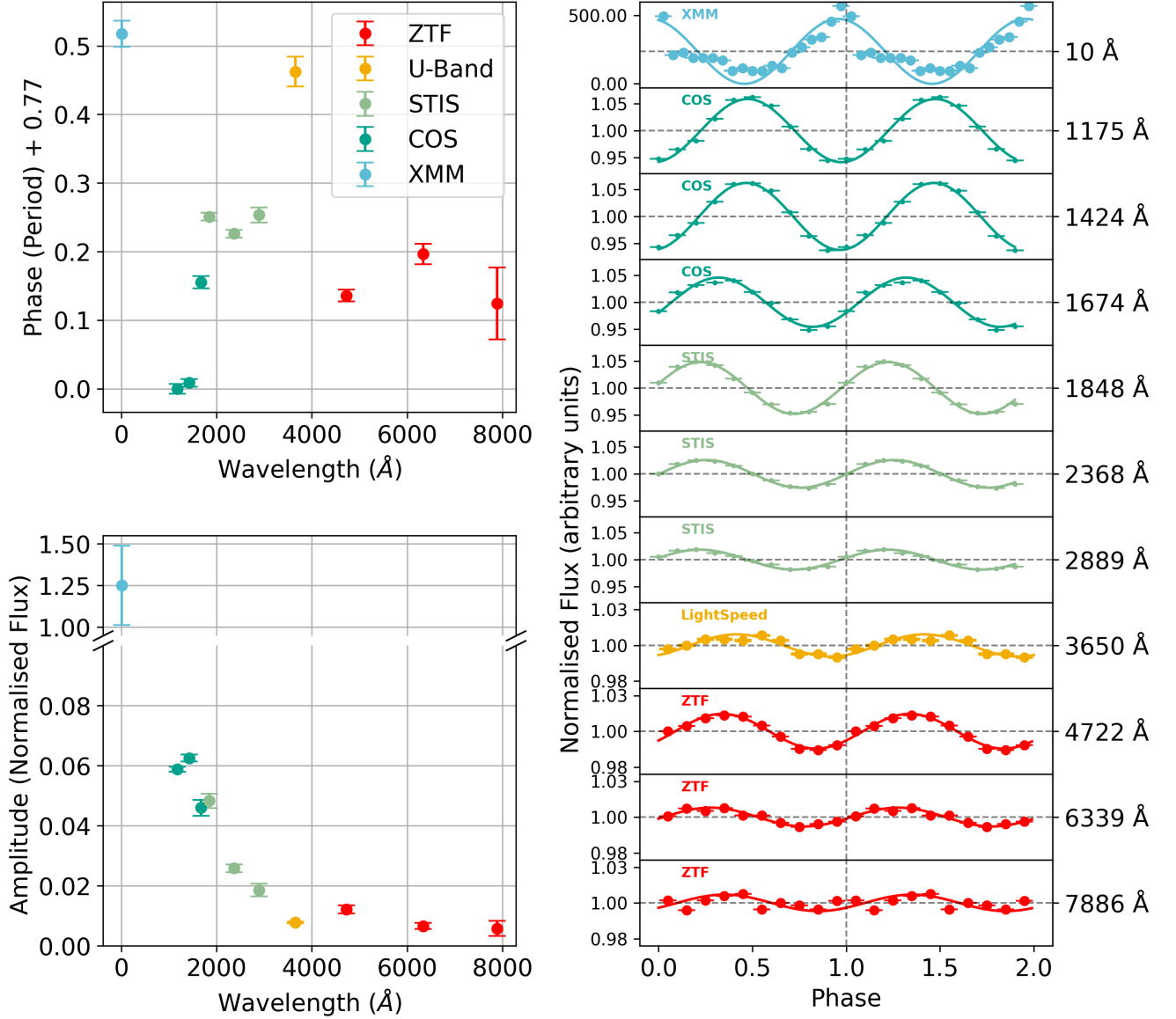


Fig. 12: **Left:** Figure showing the starting phase (top) and amplitude (bottom) of the lightcurve with respect to the Reference Ephemeris as a function of the central wavelength of the respective band. **Right:** Figure showing lightcurves in all observed bands. Apart from XMM, all lightcurves are normalised by their mean. The COS and STIS lightcurves have y-axis limits of (0.92,1.08), while the LightSpeed and ZTF lightcurves have y-axis limits of (0.97,1.03).

One possibility would be that some ionised gas is extracted from the surface of the WD itself. Because of the low temperature and extreme surface gravity of the WD, a radiative or line-driven wind would be impossible (see e.g. Vennes et al. 1988; Unglaub, K. 2008); however, the rapidly-rotating magnetic field could potentially drive a small outflow. In fact, the footprint on the surface of the WD of the open field lines that reach the

light cylinder<sup>7</sup> is not negligible (for a dipolar structure, the polar cap radius would be about 30 km, following Goldreich & Julian 1969). The potential difference along these open field lines, if there was a vacuum around the star, would be of the order of  $\sim 10^{11}$  V; this means that some ionised gas is likely extracted

<sup>7</sup> The light cylinder is defined as the distance from the rotation axis of the WD at which the corotation velocity becomes equal to the speed of light. Magnetic field lines that reach the light cylinder cannot close back to the surface of the WD.



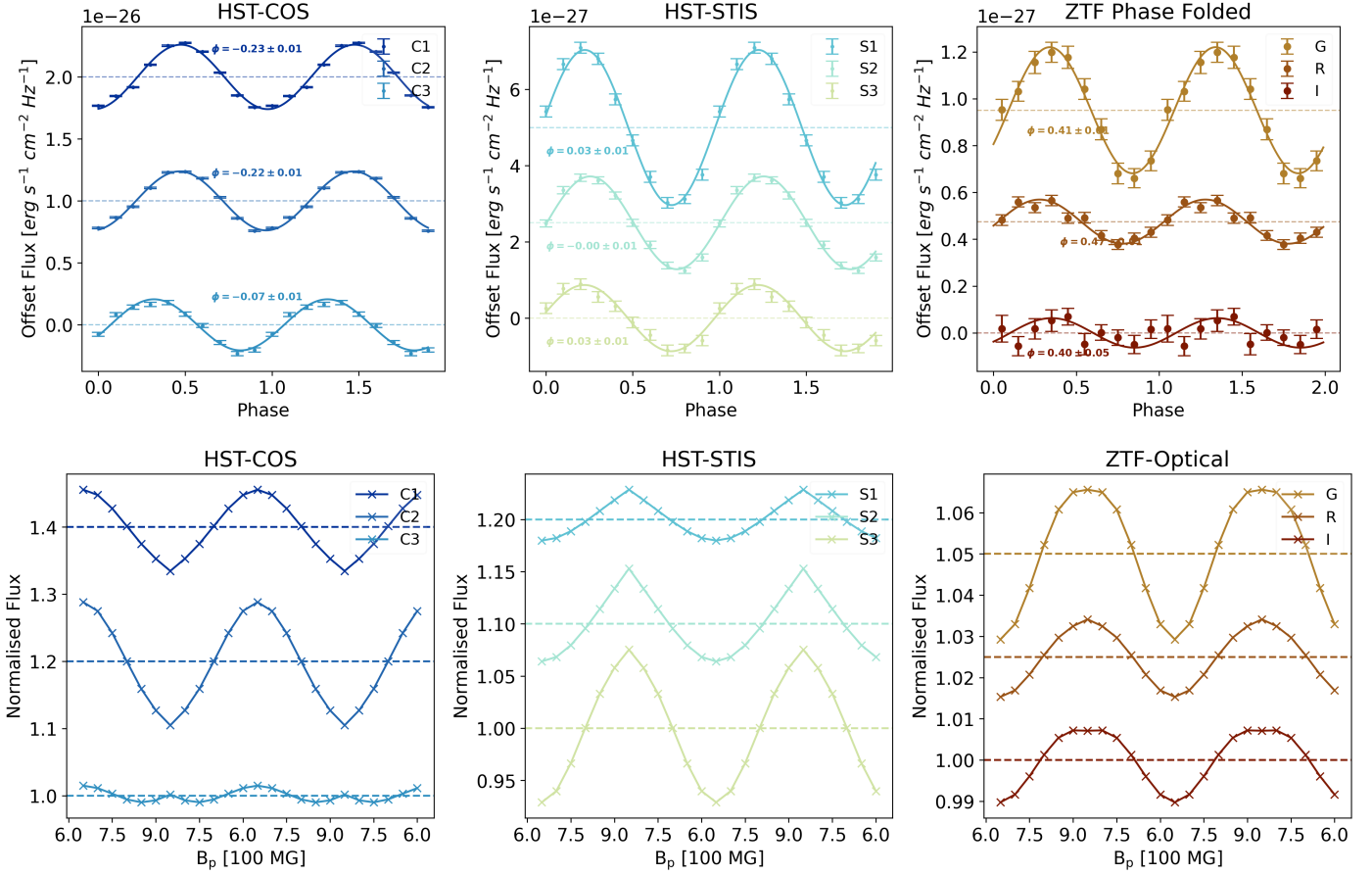


Fig. 13: **Top:** Phase-folded and normalised light curves in the different bands. The phase is defined with respect to the reference ephemeris. The ZTF light curves are in the right-most panel, while the HST light curves for COS and STIS are in the left and middle panels, respectively. **Bottom:** Flux variation as a function of magnetic field strength constructed for different spectral bands (defined above and earlier) using our magnetic atmosphere models (at constant temperature  $T_{\text{eff}} \approx 28,000\text{K}$ , same as in Fig. 5). The flux is normalised and offset in each band. Although these variations do not correspond to a real ‘lightcurve’, they qualitatively demonstrate the effect of magnetic dichroism by approximating the amplitude and phase variations seen across the different spectral bands. Since the field geometry varies across J1901’s rotational phases, these ‘lightcurves’ —constructed from a static geometry—are not intended for quantitative comparison with the observed lightcurves.

from the surface of the WD in a magnetically-driven wind. Available studies on magnetically-driven winds are mainly focused on main sequence and evolved stars and mostly on how the field accelerates winds that are powered by other mechanisms, as radiation or reconnections (Weber & Davis 1967; Belcher & MacGregor 1976; Goldreich & Julian 1970; Thirumalai & Heyl 2010; Vidotto et al. 2014; Johnstone 2017). No studies are available that examine what the steady state of a wind in the case of an extreme and old object like J1901 would look like (for the classical Weber & Davis 1967 model, the three critical points in the solution lie outside the light cylinder for J1901). Recent MHD studies aimed at modelling IRAS 00500+6713, the stellar remnant of the historical supernova 1181 (Gvaramadze et al. 2019; Ritter et al. 2021; Schaefer 2023; Lykou et al. 2023; Fesen et al. 2023; Cunningham et al. 2024), show that strong winds can be sustained in the early post-merger stages, when the remnant WD is extremely hot and nuclear burning might still be dominating the energy budget (Kashiyama et al. 2019; Zhong et al. 2023; Ko et al. 2024). Although the exact origins of the star remain contested (see Oskinova et al. 2020; Fischer et al. 2025), current literature strongly suggests that it is the remnant of a failed type Ia supernova, resulting in a partially exploded WD. The

wind from the IRAS 00500+6713 masks any spectral features that might indicate rapid rotation or a magnetic field, and thus its long-term evolution remains unclear. In the case of J1901, estimating whether the rapidly rotating field can sustain a significant outflow from the surface of the WD, this late into its evolution, would require a self-consistent MHD simulation, which is beyond the scope of this paper. However, if we assume that a small outflow can be extracted and accelerated by the field at the expenses of the rotation energy of the WD, this could explain the observed X-rays, as shocks could arise within the wind, or the pressure of the wind on the magnetosphere could lead to reconnections (we analyse possible emission mechanisms in Section 4.5).

We note that in a previous study on J1901 and other highly magnetised WDs (Bamba et al. 2024), it has been suggested that the X-ray emission in these objects is due to curvature radiation from electrons accelerated to relativistic speeds along magnetic field lines. In this model, electrons are extracted from the stellar surface under the influence of the electric potential differences along open field lines and accelerated to TeV energies in vacuum, similar to the mechanism powering the X-ray emission in pulsars. In the case of pulsars, however, a gap is formed out-

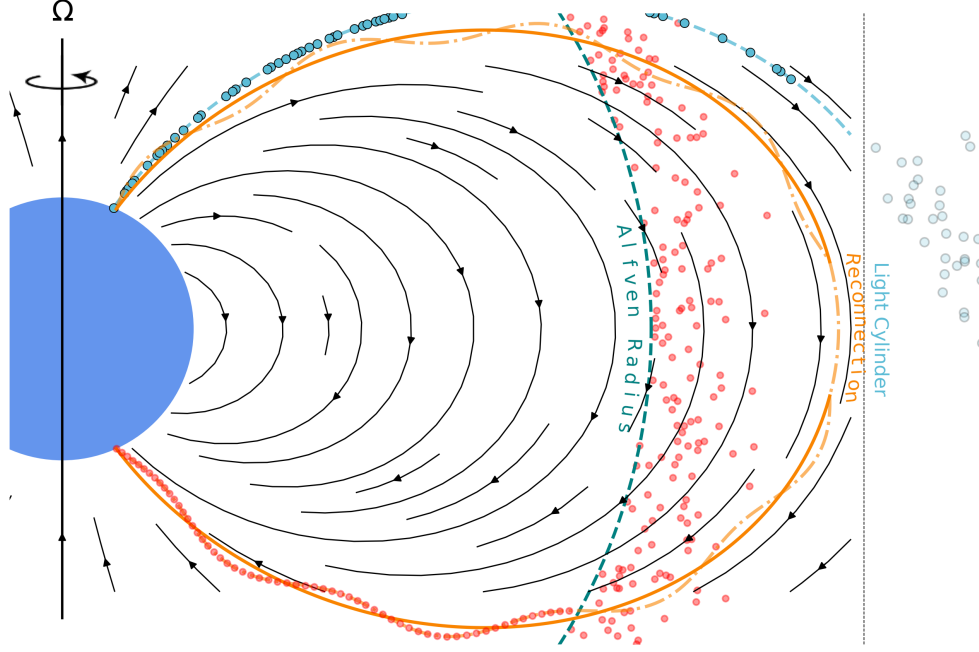


Fig. 14: Figure illustrating a possible setup (not to scale) of J1901 in blue, with dipolar field lines emanating from the poles. The Alfvén radius and Light cylinder radii are marked with dashed lines. In red is material that existed as a disk just after the merger, which is falling back. Once it crosses the Alfvén radius, it follows the field line. In blue is the extraction process due to the potential difference across the open field line at the light cylinder. In orange is a field line that is reconnecting close to the light cylinder. Along this field line, the dashed-dotted orange wiggles represent the Alfvén wave due to the reconnection. We caution the reader that while the Alfvén radius in the figure corresponds to a higher accretion rate than the rate derived from the X-rays, in which case the Alfvén radius would be outside the light cylinder.

side the neutron star surface because it is hard to extract ions from the degenerate and crystallised crust, and relativistic currents are thought to be generated when the vacuum is broken and electron-positron pairs are created (see e.g. Ruderman & Sutherland 1975). The surface of a WD, on the other hand, is made of partly ionised gas, from which it would not be possible to extract only electrons, as ions would follow. We therefore do not expect there to be relativistic electron currents in a vacuum above the surface of the WD, but rather, as we explain above, a gentle outflow of plasma. Whether this outflow could be significant enough to be the source of the observed X-rays remains to be demonstrated.

An alternative explanation for the observed X-rays is the infall of material from outside the magnetosphere of the WD. In the next section, we explore possible origins of this material. Because of the extreme magnetic field and the rapid rotation, infalling material toward the WD would be mostly ejected in a propeller mechanism, as it is seen in WD propellers like AE Aquarii and in transitional pulsars (see e.g. Wynn et al. 1997; Eracleous & Horne 1996; Campana et al. 2018; Papitto & de Martino 2022). In fact, the high field forces ionised gas to follow magnetic field lines in the region close to the WD, within the magnetospheric radius, which is usually taken as a fraction  $\xi$  of the Alfvén radius (Pringle & Rees 1972; Ghosh & Lamb 1979; Papitto & de Martino 2022).

$$\begin{aligned} R_m &\approx \xi R_A \approx \xi \left( \frac{B_p^2 R_{WD}^6}{\dot{M} \times \sqrt{2GM_{WD}}} \right)^{\frac{2}{7}} \\ &\approx 700 R_{WD} \left( \frac{\xi}{0.5} \right) \left( \frac{B_p}{800 \text{ MG}} \right)^{\frac{4}{7}} \left( \frac{R_{WD}}{2600 \text{ km}} \right)^{\frac{12}{7}} \\ &\quad \times \left( \frac{M_{WD}}{1.3 M_\odot} \right)^{-\frac{1}{7}} \left( \frac{\dot{M}}{10^{16} \text{ g/s}} \right)^{-\frac{2}{7}} \end{aligned} \quad (8)$$

where  $B_p$  is the magnetic field at the surface and  $\dot{M}$  is the mass infall rate at the magnetospheric radius. Even at a relatively high infall rate of  $10^{16}$  g/s, the magnetospheric radius is seven hundreds of WD radii. At these large radii, the centripetal acceleration of corotating material is much larger than the centripetal attraction due to gravity. These two forces become equal at the Keplerian corotation radius, which is much smaller than the Alfvén radius:

$$R_K = \left( \frac{GM_{WD}}{\Omega^2} \right)^{\frac{1}{3}} \approx 35 R_{WD} \left( \frac{P}{6.9 \text{ min}} \right)^{\frac{2}{3}} \left( \frac{M_{WD}}{1.3 M_\odot} \right)^{\frac{1}{3}}. \quad (9)$$

Taken together, the large separation between  $R_m$  and  $R_K$  places J1901 firmly in the *propeller* regime: most ionised gas that penetrates the extended magnetosphere is centrifugally expelled long before it can reach the stellar surface. Three-dimensional magnetohydrodynamic simulations of white-dwarf propellers show that strong shocks and magnetic reconnection layers develop at this magnetospheric radius, naturally producing X-ray emission with luminosities  $L_X \sim 10^{26} - 10^{28} \text{ erg s}^{-1}$  and power-law indices

$\Gamma \approx 2-3$ ; values that are consistent with our spectral fits for J1901 (Wynn et al. 1997; Romanova et al. 2005, 2012, 2018; Lii et al. 2014; Bozzo et al. 2018; Blinova et al. 2019). In Section 4.5 we explore possible X-ray emission mechanisms.

#### 4.4. Origin of the infalling material

As J1901 is most likely a WD merger remnant, a possible explanation for the presence of circumstellar material would be the fallback of bound material ejected during the merger event. Simulations of double WD mergers predict that right after the merger, the remnant WD is surrounded by a thick disk and an extended tidal tail (Guerrero et al. 2004; Lorén-Aguilar et al. 2009; Dan et al. 2014). The material in the disk is expected to be accreted on a viscous timescale, while material at high eccentricity in the bound tails accretes at longer timescales, with the fallback accretion rate predicted to decline as a power law, roughly as  $\dot{M} \propto t^{-5/3}$  (see e.g. Rosswog 2007; Lorén-Aguilar et al. 2009; Ishizaki et al. 2021). For a system with a cooling age of several hundred Myr, the corresponding accretion rate is extremely low, consistent with our X-ray luminosity estimates. However, most available simulations have only analysed the first few minutes or days after the merger, and no studies have been performed to explore if a very low level of accretion could still be ongoing hundreds of Myr after the merger.

An alternative source of material could come from the remnants of the planetary system surrounding the WD. Over a quarter of WDs show evidence of accretion of planetary material as their optical and UV spectra show the presence of metals in their atmosphere (the so-called “polluted” or “planetary-enriched” WDs; Koester et al. 2014; Zuckerman et al. 2003, 2010; Ould Rouis et al. 2024). Due to their high surface gravity, WD spectra usually only show the lightest element present (most commonly hydrogen or helium), as heavier elements sink quickly out of the observable layers; thus, the presence of metals in the spectra of polluted WDs indicates recent accretion of debris from planetary bodies (e.g. Zuckerman et al. 2007; Xu et al. 2017; Vanderburg et al. 2015; Gänsicke et al. 2019; Manser et al. 2019).

In the commonly accepted scenario for polluted WDs, the mass-loss of the central star in the last stages of the asymptotic giant branch (AGB) disrupts the orbits of the surrounding planetary system, causing the scattering of planetary bodies (asteroids, comets, small planets) to high eccentricities, where they can be tidally disrupted by the WD (for a review, see Veras 2021; Veras et al. 2024). In the case of J1901, if a populated planetary system surrounded the original stellar binary, it has now undergone several disrupting events, possibly including one or two common-envelope events, two AGB phases and a double-white-dwarf merger. No studies have been performed to analyse the combined effects of such events on the dynamics of a planetary system, and it is not clear if a reservoir of planetary objects can survive through all of them to the final merger remnant stage. However, it is known that accretion of planetary material onto the surface of a WD can power the emission of soft X-rays; indeed, X-rays have been detected from the prototypical polluted WD G 29–38 (Cunningham et al. 2022), and the accretion rate needed to power the X-ray emission in G 29–38 is very similar to the one needed for J1901 ( $\approx 10^9 \text{ g s}^{-1}$ ). Contrary to G 29–38, however, J1901 does not show any prominent metal absorption features in its spectrum, and its SED does not present any infrared excess, which indicates the presence of a dusty debris disk. Regarding the latter, we do not expect a debris disk to be close enough to the WD to emit in the near infrared, because it would be disrupted by the strong magnetic field, while metal

lines in the spectrum could be easily washed away by magnetic broadening. Future observations (for example, deep mid-infrared imaging or spectroscopy with the JWST) could detect the faint signature of a disk at a larger distance from the WD.

Because the X-ray emission is so faint, Bondi accretion from the local ISM could be another source of material. However, J1901 is remarkably close to Earth at  $\approx 40 \text{ pc}$ , so it lies in the so called Local Bubble, a region surrounding the Solar system where the ISM densities are very low ( $\sim 0.1 \text{ cm}^{-3}$ , see Cox & Reynolds 1987; Frisch et al. 2011). Using the expression for Bondi accretion rate from Wesemael (1979), assuming nominal WD velocities in the local neighbourhood ( $\approx 30 \text{ km/s}$ , consistent with the Gaia proper motion of J1901), we obtain an accretion rate of  $\sim 10^8 \text{ g/s}$  from the ISM. If we convert the observed X-ray luminosity of J1901 into an accretion rate by assuming that half of the gravitational energy of the infalling material is emitted in X-rays that we can detect (Patterson & Raymond 1985), we find a lower limit on the accretion rate of  $\dot{M} \sim 10^9 \text{ g/s}$ . Since we expect most of the infalling material to be ejected in a propeller mechanism, it is unlikely that the ISM could provide the reservoir of material needed to power the X-ray emission. Furthermore, we have shown that in the twin system of J1901, ZTF J2008+4449, accretion from the ISM could not explain the observed X-rays nor the large spin derivative (Cristea et al. 2025), so we exclude the ISM as a likely explanation for the X-ray emission in J1901 as well.

#### 4.5. X-ray Emission Mechanism

We have advanced the hypothesis that the X-rays are generated by the interaction of the WD or its magnetosphere with circumstellar material, which could either be extracted from the WD itself in a magnetically-driven wind or infalling onto the WD from outside the magnetosphere. We here consider possible X-ray emission regions and mechanisms.

If some material is infalling toward the WD, we expect that most of it will be ejected in a propeller mechanism close to the magnetospheric radius, or, if the magnetospheric radius is larger than the light cylinder, close to the latter (see Section 4.3); in this case, X-rays could be produced by shock-heated plasma where the material is being accelerated. A similar mechanism has been suggested for the soft X-ray component of the WD propeller AE Aquarii (Oruru & Meintjes 2012; Kitaguchi et al. 2014). Similarly, in the case of a magnetically-driven wind, shocks could develop where the wind is detaching from the field lines (at the edge of the magnetosphere) or, if some material can flow on closed field lines, mostly equatorial shocks can develop when the material is accelerated toward the apex of closed magnetic loops (see e.g. Babel & Montmerle 1997; ud-Doula & Owocki 2002; Ud-Doula et al. 2008; ud-Doula & Nazé 2016).

Another possible X-ray emission mechanism could be magnetic reconnection. Reconnections could occur if turbulent flows or differential rotation exert stresses on the extended magnetosphere, causing field lines to tangle. Infalling or out-flowing material that is loosely bound to the field at the edge of the magnetosphere, for example, could deform the field lines, causing continuous local reconnections; these magnetic reconnections could heat the plasma to high temperatures or accelerate particles to relativistic speed and lead to synchrotron emission (as it has been suggested for the pulsed X-ray emission of the binary WD pulsar AR Scorpii, Takata et al. 2018). In this case, the overall luminosity would depend on the supply rate of particles and on the local magnetic field topology.



The X-ray emitting region could instead be close to the WD surface. For example, Alfvén waves excited by the interaction of the material with the magnetic field at the magnetospheric radius could carry energy down to the WD surface, giving rise to hotspots or local magnetic reconnections. These reconnections could be the mechanism driving the wind from the surface of the WD. Alternatively, if part of the infalling material reaches the WD surface and is accreted, a possible X-ray emission mechanism could be the release of gravitational energy of the infalling material. Even if the propeller mechanism is highly efficient, some material might be able to reach within the corotation radius and accrete onto the WD. In fact, close to the rotation axis, the centrifugal force on the material in rigid corotation with the WD is weak out to large radii; some material could therefore trickle down along the rotation axis to field lines much closer to the WD than the magnetospheric radius and accrete. In this case, the observed X-ray emission could be due to shock-heated plasma close to the surface of the WD or by hot spots, similar to what is observed in polars. If the X-rays are powered by the gravitational energy of the infalling material, we only need a small  $\dot{M} \approx 10^{-17} M_{\odot} \text{yr}^{-1}$  (or  $\dot{M} \approx 10^9 \text{ g s}^{-1}$ ) to account for the emission.

The timing analysis of the X-ray emission can provide clues on its origin. The X-ray light curve of J1901 is remarkably stable, with no significant flares or variability detected throughout the observations, suggesting a steady process. The strongly pulsed nature of the X-ray emission, with a pulse height of approximately 600%, could indicate that a large part of the X-ray emission region is being eclipsed by the WD, hinting to the emission region being relatively small and close to the WD surface. This would be consistent, for example, with the expected geometry of magnetically channelled accretion, or of hot spots on the surface of the WD. It is interesting to notice that the X-rays are almost in anti-phase with the far-UV light curve (see Fig. 12). From our magnetic models, the minimum in the far UV light curve corresponds to the highest magnetic field strength (Fig. 13), and if accretion or reconnections are happening close to the magnetic poles of the WDs, we would indeed expect the X-rays to be at maximum when the highest field on the surface is in the line of sight. A proper modelling of the magnetic field geometry (and its corresponding effect on the light curves in different bands), however, would be required to make conclusive remarks. If the emission region is far from the WD surface, the pulsed nature of the X-ray emission cannot be explained by eclipses from the WD and it could instead be caused by relativistic beaming. Reconnections could accelerate particles to relativistic speeds, or, if the magnetic field is able to confine material close to the light cylinder, the X-ray emitting material that is co-rotating with the WD could reach relativistic velocities.

In the case of the radio-pulsing WD Ar Sco, it has been suggested that the pulsed emission from radio to UV is dominated by synchrotron radiation (Marsh et al. 2016). Extending this analysis into the X-ray, Takata et al. (2018) found that the XMM-Newton phase-resolved and phase-averaged X-ray spectroscopy was consistent with optically-thin plasma emission. However, with a pulse height of 14%, the emission in Ar Sco is likely still dominated by the “out of pulse” emission even in the pulse. After removing the out-of-pulse spectrum from the X-ray spectrum, the authors report that the isolated pulse spectrum is consistent with a power law of  $\Gamma = 2.3 \pm 0.5$ . We note that this is fully consistent with the power law we measure for ZTF J1901. Unlike in the X-ray study of Ar Sco, the X-ray pulse height in ZTF J1901 is  $\approx 600\%$  and thus we should expect the in-pulse spectrum to dominate the phase-averaged spectrum.

#### 4.6. Spin Evolution

The relatively short rotation period of J1901 of  $\approx 416$  s, opens up interesting possibilities for its spin evolution. It is known from previous MHD simulations (see e.g. Dan et al. 2014; Pakmor et al. 2024), that the merger remnant is expected to rotate extremely quickly right after the merger, owing to the conservation of angular momentum of the inspiralling binary. Some studies have suggested, however, that after the merger the remnant could spin down due to powerful winds, launched during a brief “giant-like” phase, which carry away angular momentum (Schwab 2021b; Cheng & Takata 2025). The duration of this phase is very short, on the order of  $\sim 10$  to  $10^3$  years, and the final period of the WD remnant is expected to be of the order of tens of minutes.

On the other hand, Sousa et al. (2023) suggests that the spin evolution following the merger event (up to a few Myr) should be dominated by J1901’s interaction with the circumstellar disk formed during the merger (see Lorén-Aguilar et al. 2009; Dan et al. 2014). In their model, the accretion rate from the disk is initially high enough that the magnetospheric radius is smaller than the Keplerian corotation radius and the WD can accrete, leading to an increase in the spin rate. When the accretion diminishes, the WD is bound to spin down, either through a propeller regime or due to the spin-down torque of the rotating magnetic field. In the case of J1901, they assume that the disk has been depleted and that there is no more accretion of fallback material, so that the object is currently in the phase dominated by magnetic braking.

However, the detection of X-rays might change this scenario. The spin-down for a rotating uniformly magnetised sphere due to dipole radiation is given by:

$$\dot{P} = \frac{8\pi \sin^2 \alpha \mu^2}{c^3 IP}, \quad (10)$$

where  $\mu = BR_{\text{WD}}^3$  is the magnetic dipole moment,  $\alpha$  is the angle between the rotation axis and the dipole moment,  $I$  is the moment of inertia of the WD, and  $P$  is the spin period. We obtain the moment of inertia  $I$  from radial density models, made available upon request for the CO and ONe core compositions as presented in Althaus et al. (2022, 2023). In both cases, we find that the moment of inertia roughly equates to  $I \approx 0.12 M_{\text{WD}} R_{\text{WD}}^2$ . We obtain a spin-down rate of  $\dot{P} \approx 1.95 \times 10^{-14}$  s/s for both compositions. This is higher than the estimate from Williams et al. (2022) with the revised parameters owing to their assumption of a solid sphere for the moment of inertia. Assuming all the energy lost due to spin-down is directly converted to radiation, the spin-down luminosity is given by:

$$L_{\text{sd}} = \frac{4\pi^2 \dot{P} I}{P^3}. \quad (11)$$

Using the above values, we obtain a spin-down luminosity of  $L_{\text{sd}} \approx 2.4 \times 10^{29} \text{ erg s}^{-1}$  for both core compositions. This is much larger than the observed X-ray luminosity. If the X-ray emission is powered by accretion, the spin evolution could be dominated by the accretion torque, which would be expected to spin up the WD. If instead the WD behaves like a propeller, or if a wind is leaving its surface, the spin-down might be enhanced with respect to the one due to the simple magnetic torque. Our current limit on the spin variation of  $|\dot{P}| < 10^{-13} \text{ s/s}$  does not allow us to distinguish between the different scenarios, and longer monitoring of the WD’s light curve is needed to place concrete constraints.



#### 4.7. Comparison with ZTF J2008+4449 and other merger remnants

In our companion paper (Cristea et al. 2025), we describe another merger remnant that shows evidence of circumstellar material, ZTF J2008+4449 (hereafter J2008). J1901 and J2008 offer a unique opportunity to study this new type of merger remnants that appear to be close analogues, as their similarities are striking and span several key parameters:

**Rotation Periods:** Both objects exhibit exceptionally short spin periods of approximately 7 minutes (6.9 minutes for J1901, and 6.6 minutes for J2008).

**Mass:** J1901 is among the most massive WDs known, with a mass of  $\approx 1.3M_{\odot}$ , and J2008 is also massive,  $\approx 1.1M_{\odot}$ . Both masses are well above the mean for field WDs.

**Magnetic Field Strength:** Both stars possess extremely strong surface magnetic fields, in the range of  $5\text{--}9 \times 10^8$  G. Such fields are among the highest measured for WDs and are consistent with theoretical predictions that mergers can amplify magnetic fields through dynamo processes during the coalescence event. The similar field strengths, rapid rotation and high mass in both objects point to a shared formation mechanism.

**X-ray Emission:** Both J1901 and J2008 are detected as soft X-ray sources, despite being apparently isolated (i.e., they are not in binary systems with mass-transferring companions). Their X-ray spectra are very similar in shape: when fitted by a two-temperature optically thin plasma model, we recover similar temperatures (the soft component is  $kT = 0.23 \pm 0.03$  for J1901 and  $kT = 0.23^{+0.04}_{-0.03}$  for J2008, while the hard component is  $kT = 2.9^{+1.2}_{-0.8}$  for J1901 and  $kT = 3.6^{+1.0}_{-0.7}$  for J2008). Also, both show evidence for rotationally modulated X-ray emission at the stellar spin period.

However, despite these remarkable similarities, several key differences highlight their distinct evolutionary stages:

**X-ray Luminosity Disparity:** J2008 is observed to be approximately 100 times more X-ray luminous than J1901. While J1901 has an X-ray luminosity of  $L_X \approx 1.3 \times 10^{27}$  erg s $^{-1}$ , J2008 reaches  $L_X \approx 10^{29}$  erg s $^{-1}$ .

**Period derivative:** J2008 is spinning down, with a period derivative of  $\dot{P} = (1.80 \pm 0.09) \times 10^{-12}$  s/s; this is higher than the current upper limit on the period derivative in J1901 ( $|\dot{P}| < 10^{-13}$  s/s). This means that, if J1901 is also spinning down, its period derivative is at least an order of magnitude lower than for J2008.

**H $\alpha$  Emission:** J2008 exhibits Balmer (H $\alpha$  and H $\beta$ ) emission in its optical spectrum, while J1901 shows no detectable emission lines. The presence of hydrogen emission in J2008 indicates the existence of a co-rotating half ring of hydrogen-rich material trapped in the magnetosphere close to the WD (at a distance of  $\sim 20\text{--}35$  WD radii from the surface). If a similar structure is present in ZTF J1901, the density or temperature in the disk would have to be smaller, causing the emission lines to be too weak to be detected.

**Cooling Age:** J1901 has a cooling age of approximately 470 Myr, while J2008 exhibits a higher effective temperature, implying an almost ten times younger age of about 60 Myr.

Taken together, these similarities and differences could suggest that J1901 and J2008 represent two snapshots in the life cycle of similar ultramassive, highly magnetised WDs formed via double-degenerate mergers. J2008 is observed in a younger state, showing stronger X-ray emission and Balmer emission, possibly

due to a larger reservoir of circumstellar material. J1901, older by several hundred million years, has cooled and depleted its circumstellar material, resulting in weaker X-ray emission, the absence of emission lines from trapped material and smaller spin down rate. Alternatively, if the X-rays are powered by a wind, the difference in X-ray luminosity could be due to the larger mass and surface gravity of J1901, causing a weaker wind.

For comparison, in Table 4 we also present two other extreme WDs in terms of the combination of rapid rotation and high mass and magnetic field strength, RE J0317-853 and SDSS J221141.80+113604.4. RE J0317-853 was first identified as an extreme-UV source with ROSAT and characterised by Barstow et al. (1995) as a  $1.33\text{--}1.35 M_{\odot}$  WD possessing a  $\sim 340$  MG magnetic field and a 725 s rotation period, parameters later refined through phase-resolved far-UV spectroscopy, high-precision parallax, and spectropolarimetry. Long-term photometry shows a negligible spin-down rate, and a 40 ks Chandra observation provided an upper limit of  $L_X < 6 \times 10^{27}$  erg s $^{-1}$  (0.5–8 keV) (see Dessert et al. 2022), imposing one of the most stringent constraints on axion-photon conversion for such objects. SDSS J221141.80+113604.4, reported by Kilic et al. (2021), is a  $1.27 M_{\odot}$  WD with an extremely short period of 70 s, an estimated 15 MG dipolar field, and a mixed H/He atmosphere; its kinematics and modelling of post-merger spin evolution (Sousa et al. 2022) support its origin as a double-degenerate merger remnant. No pointed X-ray observations of J2211 have yet been carried out with Chandra, XMM-Newton, or NuSTAR, leaving its high-energy properties undetermined.

#### 5. Future Prospects: Deeper X-ray and Infrared Observations

Looking ahead, our findings open several avenues for future investigation. A top priority is to unravel the geometry of ZTF J1901+1458's magnetic field and accretion structure. The available spectroscopy already hints at variability in the Zeeman-split line profiles over the rotation period, suggesting an inhomogeneous field distribution across the surface. A detailed mapping of the magnetic topology would yield insight into how such an extreme field is configured (for example, whether it is predominantly dipolar or includes significant higher-order multipole components, and whether the field is offset from the centre as in some magnetic WDs; see e.g. Euchner et al. 2002). We are developing a dedicated code to model the star's phase-resolved spectra and any future polarimetric observations. This code will incorporate the full treatment of Zeeman splitting. By fitting the observed line profiles and their modulation with rotation, we aim to infer the field strength distribution and orientation (in essence, performing “magnetic tomography” of the stellar surface).

The discoveries presented here highlight the need for further, more sensitive observations across the electromagnetic spectrum to fully characterise J1901 and similar merger remnants listed in Table 4. While current X-ray observations have revealed pulsed emission and constrained the spectral shape, the low count rates limit phase-resolved spectroscopy and the detection of subtle features. Deeper exposures with *Chandra* or *XMM-Newton* would enable to analyse if the spectrum changes between the pulse and the off-pulse phases, and to better constrain the emission mechanism. It would also improve our current constraints on the pulse profile and possible evolution of the X-ray luminosity over time. Current near-IR limits exclude luminous companions, but deeper IR observations are essential to investigate faint, cool substellar companions or residual debris disks at longer wavelengths (e.g., using *JWST*/NIRCam or

Table 4: Comparison of properties for four ultramassive, highly magnetised WDs.

Property	ZTF J2008+4449 <sup>a</sup>	ZTF J1901+1458 <sup>b</sup>	RE J0317–853 <sup>c</sup>	J2211+1136 <sup>d</sup>
RA (deg)	302.060	285.386	49.315	332.857
DEC (deg)	44.826	14.968	−85.605	11.604
Distance (pc)	350	41	31	68.12
$P_{\text{rot}}$ (s)	393.34	416	725	70
$T_{\text{eff}}$ (K)	34,000	28,000	33,800	8,000
$M$ ( $M_{\odot}$ )	1.12	1.31	1.32	1.27
$\log(g)$ ( $\text{cm/s}^2$ )	8.4	9.39	9.4	9.21
$B_{\text{avg}}$ (MG)	500	721	340	15
$L_X$ ( $\text{erg s}^{-1}$ )	$2.3 \times 10^{29}$	$1.3 \times 10^{27}$	Non-Detection <sup>1</sup> .	–
H $\alpha$ emission	Yes	No	No	No
Cooling age (Myr)	< 100	480	300 <sup>2</sup> .	2,700
Notes	X-ray, H $\alpha$	X-ray, pulsed	Rapid rotator	Rapid rotator

**Notes.** <sup>1</sup>Harayama et al. (2013) and Dessert et al. (2022) performed dedicated X-ray searches for RE J0317–853 (J0317) using *Suzaku* and *Chandra*, respectively, both reporting non-detections. <sup>2</sup> The cooling age for RE J0317–853 was calculated using the evolutionary models of Althaus et al. (2022) for the parameters reported by Vennes et al. (2003).

**References:** <sup>a</sup>Cristea et al. (2025), <sup>b</sup>this work, <sup>c</sup>Vennes et al. (2003), <sup>d</sup>Kilic et al. (2023).

MIRI). Such observations could help detect or constrain thermal emission from fallback disks or planetary debris. Additionally, monitoring for variability or transient IR excesses could reveal episodic accretion events or dust production.

## 6. Conclusions

Our multi-wavelength campaign on the ultramassive, highly magnetised WD ZTFJ1901+1458 has refined its fundamental parameters and has revealed a self-consistent picture in which the star is an *isolated*, rapidly spinning merger remnant with high-energy emission powered by the interplay between rotational energy and a tenuous supply of circumstellar plasma.

The *HST* UV spectra, analysed with a newly developed set of magnetised atmosphere models, show Zeeman-split Lyman absorption features and a strong spectral break at  $\sim 3000$  Å. Although we currently lack a full grid of models able to properly characterize the structure of the magnetic field of the WD, the new models are able to capture most of the features of the broad-band spectrum of the WD. The best-fit solution yields an effective temperature  $T_{\text{eff}} = 28\,060 \pm 20$  K, a radius  $R = 2\,634 \pm 10$  km, and a polar magnetic field strength of  $B_p \approx 1.06 \times 10^9$  G. Employing WD evolutionary models, we derive a mass  $M = 1.30 \pm 0.01 M_{\odot}$  and a cooling age of 460–490 Myr (Althaus et al. 2022). Compared with the previous estimate, the star is  $\sim 25\%$  larger, moving its size from “Moon-sized” to “Titan-sized” while placing its central density close to but below the sodium electron-capture threshold. It is therefore unlikely that the WD is currently undergoing Urca cooling in its core, as previously suggested in C21 and Schwab (2021a).

Near-infrared photometry and spectroscopy from UKIDSS and FIRE align precisely with the WD continuum and show *no* excess at  $1\text{--}2.5 \mu$ ; any stellar or substellar companion hotter than  $\approx 700$  K would present a detectable excess in the data. By computing irradiation temperatures along brown-dwarf evolutionary tracks, we rule out Roche-lobe-filling brown dwarf companions of all plausible masses and ages, confirming that J1901 is isolated, and the observed X-rays cannot be due to accretion from a binary companion in a CV system (a cold planet or a more dis-

tant brown dwarf transferring mass through winds would still be allowed).

A joint fit to the *Chandra*/ACIS-I and *XMM-Newton*/EPIC spectra favours a single power-law model of photon index  $\Gamma = 2.9^{+0.4}_{-0.3}$  over a two-temperature isothermal plasma model with Solar abundance and temperatures  $kT = 0.23 \pm 0.03$  K and  $kT = 2.95^{+1.23}_{-0.81}$  K. The 0.25–10 keV luminosity is  $(1.3 \pm 0.2) \times 10^{27} \text{ erg s}^{-1}$  and is modulated with a  $\approx 600\%$  pulse fraction on the 6.94-min rotation period. The spectral shape is inconsistent with photospheric emission from the WD, and thus the X-ray emission is likely due to the interaction of the WD or its magnetosphere with circumstellar material.

We have considered three possible sources of circumstellar material, but further studies are needed to verify if any of them are consistent with the observations:

1. *Fallback accretion.* Merger simulations predict that material ejected on eccentric orbits during the merger event could fall back and accrete onto the WD on long timescales. As J1901 is most likely a merger remnant, a reservoir of circumstellar material could be provided by the fallback of bound ejecta, although no simulations have explored such long timescales, and it is not clear if a low level of fallback accretion is still possible hundreds of Myrs after the merger.
2. *Disrupted planetary body.* A reservoir of circumstellar material could be created by the tidal disruption of a planetary body, like a comet, an asteroid or a small planet. Such tidal disruptions of rocky bodies on high-eccentricity orbits are common around normal WDs, and X-rays from accretion of planetary material consistent with the ones detected in J1901 have recently been observed from a polluted WD (Cunningham et al. 2022). No current studies however, have explored the dynamical effects of a double WD merger on a planetary system, and it is not clear if a reservoir of planetary bodies could have survived the evolution of the system.
3. *Magnetically driven wind.* A small plasma outflow lifted from the stellar surface along open field lines could form internal shocks or disturb the magnetosphere, inducing reconnections, yielding X-rays. The necessary energy would be drawn from the white-dwarf rotational energy. No studies

Table 5: Summary of measured and derived parameters for ZTF J1901+1458.

Origin	Parameter	Value
From Gaia DR3	Gaia ID	4506869128279648512
	Parallax	$24.1538 \pm 0.0489$ mas
	Distance <a href="#">Gaia Collaboration (2020)</a>	$41.44 \pm 0.08$ pc
From SED Fitting	Radius of the WD	$2630 \pm 10$ km
	Temperature of the WD	$T_{\text{eff}} = 28015 \pm 20$ K
	Mass of the WD	$1.31 \pm 0.01 M_{\odot}$ [CO], $1.29 \pm 0.01 M_{\odot}$ [ONe]
	Cooling age of the WD	$0.49 \pm 0.01$ Gyr [CO], $0.46 \pm 0.01$ Gyr [ONe]
	Extinction toward the WD	$E(B-V) = (0.0 \pm 1.0) \times 10^{-5}$
From light curve analysis	Spin period of the WD	$P_0 = 6.9373843 \pm 0.0000001$ min
	Period derivative (3- $\sigma$ upper bound)	$ \dot{P}  < 10^{-13}$ s/s
From X-rays analysis	X-ray luminosity in the 0.25–10.0 keV band	$L_X = 1.28^{+0.18}_{-0.15} \times 10^{27}$ erg s $^{-1}$
	Power law index	$\Gamma = 2.9^{+0.4}_{-0.3}$
	2-temperature model	$kT_1 = 2.95^{+1.23}_{-0.81}$ keV $kT_2 = 0.23 \pm 0.03$ keV
	Pulse fraction	600% peak/quiescence

have been performed on magnetically driven winds in such an extreme regime, however, and it is not clear if the rotating magnetic field could successfully extract a sizeable wind from the surface of the WD.

Because of the large gap between the magnetospheric radius ( $R_m \approx 500 R_{\text{WD}}$ ) and the Keplerian corotation radius ( $R_K \approx 35 R_{\text{WD}}$ ), any infalling material is likely to be centrifugally propelled away as soon as it gets close enough to the star to feel the effect of the magnetic field. In this case, shock-heated plasma could be the source of emission close to the ejection region. Alternatively, the pressure exerted by the infalling or outflowing gas (in case of a wind) on the magnetosphere could cause reconnections either at the ejection region or close to the surface. The large pulse fraction of the X-rays hints to either the eclipsing of part of the emission region by the WD or to relativistic beaming, and the clear phase offset between the X-ray and far-UV light curves hints that at least part of the emission zone resides above the surface.

In our companion paper ([Cristea et al. 2025](#)), we present the discovery of another isolated merger remnant (ZTF J2008+4449) with very similar physical properties to J1901 (high mass, strong field, short rotation period) and very similar X-ray emission characteristics. The discovery of two rapidly rotating and highly magnetised WDs showing high-energy emission opens the possibility of a new class of merger remnants interacting with circumstellar material. As more merger remnants are being found thanks to time-domain and spectroscopic surveys, future X-ray campaigns could reveal more systems in this new class, shedding light on their physics and evolution.

*Acknowledgements.* We thank Lynne Hillenbrand, Srijan Bharati Das, Samarth Hawaldar, CP Johnstone and Soumyadeep Bhattacharjee for helpful discussions. IC was supported by NASA through grants from the Space Telescope Science Institute, under NASA contracts NASA.22K1813, NAS5-26555 and NAS5-03127. TC was supported by NASA through the NASA Hubble Fellowship grant HST-HF2-51527.001-A awarded by the Space Telescope Science Institute, which is operated by the Association of Universities for Research in Astronomy, Inc., for NASA, under contract NAS5-26555. IT acknowledges the support by Deutsches Zentrum für Luft- und Raumfahrt (DLR) through grant 50 OX 2301. This project has received funding from the European Research Council (ERC) under the European Union’s Horizon 2020 research and innovation programme (Grant agreement No. 101020057). This work was based on observations obtained with the Samuel Oschin Telescope 48-inch and the 60-inch Telescope at the Palomar Observatory as part of the Zwicky Transient Facility project. ZTF is supported by the National Science Foundation under Grants No. AST-1440341, AST-2034437, and currently Award #2407588. ZTF receives additional funding from the ZTF partnership. Current members include Caltech, USA; Caltech/IPAC, USA; University of Maryland, USA; University of California, Berkeley, USA; University of Wisconsin at Milwaukee, USA; Cornell University, USA; Drexel University, USA; University of North Carolina at Chapel Hill, USA; Institute of Science and Technology, Austria; National Central University, Taiwan, and OKC, University of Stockholm, Sweden. Operations are conducted by Caltech’s Optical Observatory (COO), Caltech/IPAC, and the University of Washington at Seattle, USA. This work has made use of data from the European Space Agency (ESA) mission *Gaia* (<https://www.cosmos.esa.int/gaia>), processed by the *Gaia* Data Processing and Analysis Consortium (DPAC, <https://www.cosmos.esa.int/web/gaia/dpac/consortium>). Funding for the DPAC has been provided by national institutions, in particular the institutions participating in the *Gaia* Multilateral Agreement. This paper includes data gathered with the 6.5 meter Magellan Telescopes located at Las Campanas Observatory, Chile. The Pan-STARRS1 Surveys (PS1) and the PS1 public science archive have been made possible through contributions by the Institute for Astronomy, the University of Hawaii, the Pan-STARRS Project Office, the Max-Planck Society and its participating institutes, the Max Planck Institute for Astronomy, Heidelberg and the Max Planck Institute for Extraterrestrial Physics, Garching, The Johns Hopkins University, Durham University, the University of Edinburgh, the Queen’s University Belfast, the Harvard-Smithsonian Center for Astrophysics, the Las Cumbres Observatory Global Telescope Network Incorporated, the National Central University of Taiwan, the Space Telescope Science Institute, the



National Aeronautics and Space Administration under Grant No. NNX08AR22G issued through the Planetary Science Division of the NASA Science Mission Directorate, the National Science Foundation Grant No. AST-1238877, the University of Maryland, Eotvos Lorand University (ELTE), the Los Alamos National Laboratory, and the Gordon and Betty Moore Foundation. This work made use of Astropy<sup>8</sup>, a community-developed core Python package and an ecosystem of tools and resources for astronomy (Astropy Collaboration et al. 2013, 2018, 2022). This work made use of the perceptually uniform olormaps from Fabio Crameri (Crameri 2023). This research was supported by the Scientific Service Units (SSU) of IST Austria through resources provided by Scientific Computing (SciComp).

## References

- Achilleos, N. & Wickramasinghe, D. T. 1989, *ApJ*, 346, 444
- Althaus, L. G., Camisassa, M. E., Torres, S., et al. 2022, *A&A*, 668, A58
- Althaus, L. G., Córscico, A. H., Camisassa, M. E., et al. 2023, *MNRAS*, 523, 4492
- Althaus, L. G., Gil-Pons, P., Córscico, A. H., et al. 2021, *A&A*, 646, A30
- Arnaud, K. A. 1996, in *Astronomical Society of the Pacific Conference Series*, Vol. 101, *Astronomical Data Analysis Software and Systems V*, ed. G. H. Jacoby & J. Barnes, 17
- Asplund, M., Grevesse, N., Sauval, A. J., & Scott, P. 2009, *ARA&A*, 47, 481
- Astropy Collaboration, Price-Whelan, A. M., Lim, P. L., et al. 2022, *ApJ*, 935, 167
- Astropy Collaboration, Price-Whelan, A. M., Sipőcz, B. M., et al. 2018, *AJ*, 156, 123
- Astropy Collaboration, Robitaille, T. P., Tollerud, E. J., et al. 2013, *A&A*, 558, A33
- Babel, J. & Montmerle, T. 1997, *A&A*, 323, 121
- Bailer-Jones, C. A. L., Rybizki, J., Fournesneau, M., Demleitner, M., & Andrae, R. 2021, *AJ*, 161, 147
- Bamba, A., Terada, Y., Kashiya, K., et al. 2024, On the X-ray efficiency of the white dwarf pulsar candidate ZTF J190132.9+145808.7
- Barstow, M. A., Jordan, S., O'Donoghue, D., et al. 1995, *MNRAS*
- Belcher, J. W. & MacGregor, K. B. 1976, *ApJ*, 210, 498
- Bellm, E. C., Kulkarni, S. R., Graham, M. J., et al. 2019, *PASP*, 131, 018002
- Blatman, D. & Ginzburg, S. 2024, *MNRAS*, 533, L13
- Blinova, A. A., Romanova, M. M., Ustyugova, G. V., Koldoba, A. V., & Lovelace, R. V. E. 2019, *MNRAS*, 487, 1754
- Bozzo, E., Ascenzi, S., Ducci, L., et al. 2018, *A&A*, 617, A126
- Bradley, L., Sipőcz, B., Robitaille, T., et al. 2024, *astropy/photutils: 2.0.2*
- Brent, R. P. 1973, *Algorithms for Minimization without Derivatives* | BibSonomy
- Buchner, J. 2016, *Astrophysics Source Code Library*
- Buchner, J., Georgakakis, A., Nandra, K., et al. 2014, *A&A*, 564, A125
- Burdge, K. in prep
- Burleigh, M. R., Jordan, S., & Schweizer, W. 1999, *ApJ*, 510, L37
- Caiazzo, I., Burdge, K., Ferrario, L., et al. 2021, The radius and magnetic field structure of the smallest white dwarf, HST Proposal. Cycle 29, ID. #16753
- Caiazzo, I., Burdge, K. B., Fuller, J., et al. 2021, *Nature*, 595, 39–42
- Campana, S., Stella, L., Mereghetti, S., & de Martino, D. 2018, *A&A*, 610, A46
- Carnall, A. C. 2017, *SpectRes: A Fast Spectral Resampling Tool in Python*
- Cash, W. 1979, *ApJ*, 228, 939
- Chambers, K. C., Magnier, E. A., Metcalfe, N., et al. 2019, *The Pan-STARRS1 Surveys*
- Charpinet, S., Fontaine, G., & Brassard, P. 2009, *Nature*, 461, 501
- Cheng, Y. & Takata, J. 2025, Spin evolution modeling for a newly-formed white dwarf resulting from binary white dwarf merger
- Cox, D. P. & Reynolds, R. J. 1987, *Annual Review of Astronomy and Astrophysics*, 25, 303
- Crameri, F. 2023, *Scientific colour maps*
- Cristea, A. A., Caiazzo, I., Cunningham, T., et al. 2025, *arXiv e-prints*, *arXiv:2507.13850*
- Cunningham, T., Caiazzo, I., Prusinski, N. Z., et al. 2024, *ApJ*, 975, L7
- Cunningham, T., Wheatley, P. J., Tremblay, P.-E., et al. 2022, *Nature*, 602, 219
- Dan, M., Rosswog, S., Brüggen, M., & Podsiadlowski, P. 2014, *MNRAS*, 438, 14
- Dekany, R., Smith, R. M., Riddle, R., et al. 2020, *PASP*, 132, 038001
- Dessert, C., Long, A. J., & Safdi, B. R. 2019, *Phys. Rev. Lett.*, 123, 061104
- Dessert, C., Long, A. J., & Safdi, B. R. 2022, *Phys. Rev. Lett.*, 128, 071102
- Dhillon, V. S., Marsh, T. R., Stevenson, M. J., et al. 2007, *MNRAS*, 378, 825
- Dominguez, I., Straniero, O., Tornambe, A., & Isern, J. 1996, *ApJ*, 472, 783
- Eracleous, M. & Horne, K. 1996, *ApJ*, 471, 427
- Euchner, F., Jordan, S., Beuermann, K., Gänsicke, B. T., & Hessman, F. V. 2002, *A&A*, 390, 633
- Ferrario, L., Vennes, S., Wickramasinghe, D. T., Bailey, J. A., & Christian, D. J. 1997a, *MNRAS*, 292, 205
- Ferrario, L., Wickramasinghe, D. T., Liebert, J., Schmidt, G. D., & Biegging, J. H. 1997b, *MNRAS*, 289, 105
- Fesen, R. A., Schaefer, B. E., & Patchick, D. 2023, *ApJ*, 945, L4
- Fischer, J. G., Halm, H., Neuhäuser, R., & Neuhäuser, D. L. 2025, *Astronomische Nachrichten*, n/a, e70024
- Fleury, L., Caiazzo, I., & Heyl, J. 2023, *Phys. Rev. D*, 107, L101303
- Foreman-Mackey, D., Hogg, D. W., Lang, D., & Goodman, J. 2013, *PASP*, 125, 306
- Fournesneau, M., Andrae, R., Dharmawardena, T., et al. 2022, *A&A*, 662, A125
- Frisch, P. C., Redfield, S., & Slavin, J. D. 2011, *Annual Review of Astronomy and Astrophysics*, 49, 237
- Fruscione, A., McDowell, J. C., Allen, G. E., et al. 2006, in *Society of Photo-Optical Instrumentation Engineers (SPIE) Conference Series*, Vol. 6270, *Observatory Operations: Strategies, Processes, and Systems*, ed. D. R. Silva & R. E. Duxsey, 62701V
- Gabriel, C., Denby, M., Fyfe, D. J., et al. 2004, in *Astronomical Society of the Pacific Conference Series*, Vol. 314, *Astronomical Data Analysis Software and Systems (ADASS) XIII*, ed. F. Ochsenbein, M. G. Allen, & D. Egret, 759
- Gaia Collaboration. 2020, *VizieR Online Data Catalog*, 1350, I/350
- Gänsicke, B. T., Schmidt, G. D., Jordan, S., & Szkody, P. 2001, *ApJ*, 555, 380
- Gänsicke, B. T., Schreiber, M. R., Toloza, O., et al. 2019, *Nature*, 576, 61
- García-Berro, E., Lorén-Aguilar, P., Aznar-Siguán, G., et al. 2012, *ApJ*, 749, 25
- García-Berro, E., Ritosca, C., & Iben, Jr., I. 1997, *ApJ*, 485, 765
- Garmire, G. P., Bautz, M. W., Ford, P. G., Nousek, J. A., & Ricker, Jr., G. R. 2003, in *Society of Photo-Optical Instrumentation Engineers (SPIE) Conference Series*, Vol. 4851, *X-Ray and Gamma-Ray Telescopes and Instruments for Astronomy*, ed. J. E. Truemper & H. D. Tananbaum, 28–44
- Ghosh, P. & Lamb, F. K. 1979, *ApJ*, 232, 259
- Goldreich, P. & Julian, W. H. 1969, *ApJ*, 157, 869
- Goldreich, P. & Julian, W. H. 1970, *ApJ*, 160, 971
- Gordon, K. D., Clayton, G. C., Decleir, M., et al. 2023, *ApJ*, 950, 86
- Graham, M. J., Kulkarni, S. R., Bellm, E. C., et al. 2019, *PASP*, 131, 078001
- Green, J. C., Froning, C. S., Osterman, S., et al. 2011, *ApJ*, 744, 60
- Green, R. F. & Liebert, J. 1981, *PASP*, 93, 105
- Guerrero, J., García-Berro, E., & Isern, J. 2004, *A&A*, 413, 257
- Gvaramadze, V. V., Gräfenr, G., Langer, N., et al. 2019, *Nature*, 569, 684
- Harayama, A., Terada, Y., Ishida, M., et al. 2013, *PASJ*, 65, 73
- Harding, L. K., Hallinan, G., Milburn, J., et al. 2016, *MNRAS*, 457, 3036
- Hardy, F., Dufour, P., & Jordan, S. 2023, *MNRAS*, 520, 6111
- Hermes, J. J., Gänsicke, B. T., Kawaler, S. D., et al. 2017, *ApJS*, 232, 23
- Hernández Santisteban, J. V., Knigge, C., Littlefair, S. P., et al. 2016, *Nature*, 533, 366
- Hulbert, S. & Hodge, P. 1997, in *The 1997 HST Calibration Workshop with a New Generation of Instruments*, 47
- Ishizaki, W., Ioka, K., & Kiuchi, K. 2021, *ApJ*, 916, L13
- Jansen, F., Lumb, D., Altieri, B., et al. 2001, *A&A*, 365, L1
- Jermyn, A. S., Tout, C. A., & Ogilvie, G. I. 2017, *MNRAS*, 469, 1768
- Jewett, G., Kilic, M., Bergeron, P., et al. 2024, *arXiv e-prints*, *arXiv:2407.04827*
- Johnstone, C. P. 2017, *A&A*, 598, A24
- Jordan, S. 1992, *A&A*, 265, 570
- Jordan, S., Wolff, B., Koester, D., & Napiwotzki, R. 1994, *A&A*, 290, 834
- Kastra, J. S. & Bleeker, J. A. M. 2016, *A&A*, 587, A151
- Kaiser, M. E., Hodge, P. E., Keyes, C., et al. 2008, in *Ground-based and Airborne Instrumentation for Astronomy II*, Vol. 7014, *SPIE*, 2238–2250
- Kashiya, K., Fujisawa, K., & Shigeyama, T. 2019, *The Astrophysical Journal*, 887, 39
- Kepler, S. O., Pelisoli, I., Jordan, S., et al. 2013, *MNRAS*, 429, 2934
- Kilic, M., Kosakowski, A., Moss, A. G., Bergeron, P., & Conly, A. A. 2021, *ApJ*, 923, L6
- Kilic, M., Moss, A. G., Kosakowski, A., et al. 2023, *MNRAS*, 518, 2341
- Kippenhahn, R., Weigert, A., & Weiss, A. 2013, *Stellar Structure and Evolution*
- Kitaguchi, T., An, H., Beloborodov, A. M., et al. 2014, *ApJ*, 782, 3
- Ko, T., Tsuna, D., Hatsukade, B., & Shigeyama, T. 2024, *Publications of the Astronomical Society of Japan*, 76, 475
- Koester, D., Dreizler, S., Weidemann, V., & Allard, N. F. 1998, *A&A*, 338, 612
- Koester, D., Gänsicke, B. T., & Farihi, J. 2014, *A&A*, 566, A34
- Kraft, R. P., Burrows, D. N., & Nousek, J. A. 1991, *ApJ*, 374, 344
- Külebi, B., Jordan, S., Euchner, F., Gänsicke, B. T., & Hirsch, H. 2009, *A&A*, 506, 1341
- Külebi, B., Jordan, S., Nelan, E., Bastian, U., & Altmann, M. 2010, *A&A*, 524, A36
- Lamb, F. K. & Sutherland, P. G. 1974, in *IAU Symposium*, Vol. 53, *Physics of Dense Matter*, ed. C. J. Hansen, 265
- Lawrence, A., Warren, S. J., Almaini, O., et al. 2007, *MNRAS*, 379, 1599
- Lii, P., Romanova, M., & Lovelace, R. 2014, in *EPJ Web of Conferences*, Vol. 64, 05002
- Liu, F. L. & Zhao, L. B. 2022, *ApJS*, 259, 47
- Lorén-Aguilar, P., Isern, J., & García-Berro, E. 2009, *A&A*, 500, 1193

<sup>8</sup> <http://www.astropy.org>



- Lothringer, J. D. & Casewell, S. L. 2020, *ApJ*, 905, 163
- Lykou, F., Parker, Q. A., Ritter, A., et al. 2023, *ApJ*, 944, 120
- Manser, C. J., Gänsicke, B. T., Eggl, S., et al. 2019, *Science*, 364, 66
- Marley, M. S., Gelino, C., Stephens, D., Lunine, J. I., & Freedman, R. 1999, *ApJ*, 513, 879
- Marley, M. S., Saumon, D., Visscher, C., et al. 2021, *ApJ*, 920, 85
- Marsh, T. R., Gänsicke, B. T., Hümmelich, S., et al. 2016, *Nature*, 537, 374
- Martin, B. & Wickramasinghe, D. T. 1979, *MNRAS*, 189, 883
- Martin, B. & Wickramasinghe, D. T. 1981, *MNRAS*, 196, 23
- Martin, B. & Wickramasinghe, D. T. 1984, *MNRAS*, 206, 407
- Masci, F. J., Laher, R. R., Rusholme, B., et al. 2019, *PASP*, 131, 018003
- Mason, K. O., Breeveld, A., Much, R., et al. 2001, *A&A*, 365, L36
- Merani, N., Main, J., & Wunner, G. 1995, *A&A*, 298, 193
- Munday, J., Pakmor, R., Pelisoli, I., et al. 2025a, *Nature Astronomy*, 9, 872
- Munday, J., Pelisoli, I., Tremblay, P.-E., et al. 2025b, *MNRAS*, 541, 3494
- Murai, T., Sugimoto, D., Hōshi, R., & Hayashi, C. 1968, *Progress of Theoretical Physics*, 39, 619
- Ning, O., Dessert, C., Hong, V., & Safdi, B. R. 2025, *Phys. Rev. D*, 111, 103002
- O'Dwyer, I. J., Chu, Y.-H., Gruendl, R. A., Guerrero, M. A., & Webbink, R. F. 2003, *AJ*, 125, 2239
- Oruru, B. & Meintjes, P. J. 2012, *MNRAS*, 421, 1557
- Oskina, L. M., Gvaramadze, V. V., Gräfenr, G., Langer, N., & Todt, H. 2020, *Astronomy and Astrophysics*, 644, L8
- Ould Rouis, L. B., Hermes, J. J., Gänsicke, B. T., et al. 2024, *ApJ*, 976, 156
- Pakmor, R., Pelisoli, I., Justham, S., et al. 2024, *A&A*, 691, A179
- Papitto, A. & de Martino, D. 2022, in *Astrophysics and Space Science Library*, Vol. 465, *Astrophysics and Space Science Library*, ed. S. Bhattacharyya, A. Papitto, & D. Bhattacharyya, 157–200
- Patterson, J. & Raymond, J. C. 1985, *ApJ*, 292, 535
- Pringle, J. E. & Rees, M. J. 1972, *A&A*, 21, 1
- Prochaska, J., Hennawi, J., Westfall, K., et al. 2020a, *The Journal of Open Source Software*, 5, 2308
- Prochaska, J. X., Hennawi, J., Cooke, R., et al. 2020b, *papeit/PypeIt: Release 1.0.0*
- Rakavy, G., Shaviv, G., & Zinamon, Z. 1967, *ApJ*, 150, 131
- Rigault, M. 2018, *Zenodo*
- Ritter, A., Parker, Q. A., Lykou, F., et al. 2021, *ApJ*, 918, L33
- Romanova, M. M., Blinova, A. A., Ustyugova, G. V., Koldoba, A. V., & Lovelace, R. V. E. 2018, *New A*, 62, 94
- Romanova, M. M., Ustyugova, G. V., Koldoba, A. V., & Lovelace, R. V. E. 2005, *ApJ*, 635, L165
- Romanova, M. M., Ustyugova, G. V., Koldoba, A. V., & Lovelace, R. V. E. 2012, *MNRAS*, 421, 63
- Rosswog, S. 2007, *MNRAS*, 376, L48
- Ruderman, M. A. & Sutherland, P. G. 1975, *ApJ*, 196, 51
- Rueda, J., Ruffini, R., Wang, Y., et al. 2019, *J. Cosmology Astropart. Phys.*, 2019, 044
- Sahu, S., Bédard, A., Gänsicke, B. T., et al. 2025, *Nature Astronomy* [[arXiv:2508.03811](https://arxiv.org/abs/2508.03811)]
- Salaris, M., Blouin, S., Cassisi, S., & Bedin, L. R. 2024, *A&A*, 686, A153
- Schaefer, B. E. 2023, *MNRAS*, 523, 3885
- Schimeczek, C. & Wunner, G. 2014, *ApJS*, 212, 26
- Schmidt, G. D., West, S. C., Liebert, J., Green, R. F., & Stockman, H. S. 1986, *ApJ*, 309, 218
- Schwab, J. 2021a, *ApJ*, 916, 119
- Schwab, J. 2021b, *ApJ*, 906, 53
- Schwab, J., Bildsten, L., & Quataert, E. 2017, *MNRAS*, 472, 3390
- Shen, K. J., Bildsten, L., Kasen, D., & Quataert, E. 2012, *ApJ*, 748, 35
- Shen, K. J., Blouin, S., & Breivik, K. 2023, *ApJ*, 955, L33
- Siess, L. 2010, *A&A*, 512, A10
- Simcoe, R. A., Burgasser, A. J., Bernstein, R. A., et al. 2008, in *Society of Photo-Optical Instrumentation Engineers (SPIE) Conference Series*, Vol. 7014, *Ground-based and Airborne Instrumentation for Astronomy II*, ed. I. S. McLean & M. M. Casali, 70140U
- Simcoe, R. A., Burgasser, A. J., Bochanski, J. J., et al. 2010, in *Society of Photo-Optical Instrumentation Engineers (SPIE) Conference Series*, Vol. 7735, *Ground-based and Airborne Instrumentation for Astronomy III*, ed. I. S. McLean, S. K. Ramsay, & H. Takami, 773514
- Sousa, M. F., Coelho, J. G., de Araujo, J. C. N., Guidorzi, C., & Rueda, J. A. 2023, *ApJ*, 958, 134
- Sousa, M. F., Coelho, J. G., de Araujo, J. C. N., Kepler, S. O., & Rueda, J. A. 2022, *ApJ*, 941, 28
- Strider, L., Briel, U., Dennerl, K., et al. 2001, *A&A*, 365, L18
- Sullivan, P. W. & Simcoe, R. A. 2012, *Publications of the Astronomical Society of the Pacific*, 124, 1336
- Takata, J., Hu, C. P., Lin, L. C. C., et al. 2018, *ApJ*, 853, 106
- Thirumalai, A. & Heyl, J. S. 2010, *MNRAS*, 409, 1669
- Tout, C. A., Wickramasinghe, D., Liebert, J., Ferrario, L., & Pringle, J. 2008, *MNRAS*, 387, 897
- Tremblay, P.-E., Ludwig, H.-G., Steffen, M., & Freytag, B. 2013, *A&A*, 559, A104
- Turner, M. J. L., Abbey, A., Arnaud, M., et al. 2001, *A&A*, 365, L27
- ud-Doula, A. & Nazé, Y. 2016, *Advances in Space Research*, 58, 680
- ud-Doula, A. & Owocki, S. P. 2002, *ApJ*, 576, 413
- Ud-Doula, A., Owocki, S. P., & Townsend, R. H. D. 2008, *MNRAS*, 385, 97
- Unglaub, K. 2008, *A&A*, 486, 923
- Vanderburg, A., Johnson, J. A., Rappaport, S., et al. 2015, *Nature*, 526, 546
- Vennes, S. 1999, *ApJ*, 525, 995
- Vennes, S., Pelletier, C., Fontaine, G., & Wesemael, F. 1988, *ApJ*, 331, 876
- Vennes, S., Schmidt, G. D., Ferrario, L., et al. 2003, *ApJ*, 593, 1040
- Veras, D. 2021, in *Oxford Research Encyclopedia of Planetary Science*, 1
- Veras, D., Mustill, A. J., & Bonsor, A. 2024, *Reviews in Mineralogy and Geochemistry*, 90, 141
- Vidotto, A. A., Gregory, S. G., Jardine, M., et al. 2014, *MNRAS*, 441, 2361
- Vito, F., Brandt, W. N., Ricci, F., et al. 2021, *Astronomy and Astrophysics*, 649, A133
- Weber, E. J. & Davis, Jr., L. 1967, *ApJ*, 148, 217
- Weisskopf, M. C., Tananbaum, H. D., Van Speybroeck, L. P., & O'Dell, S. L. 2000, in *Society of Photo-Optical Instrumentation Engineers (SPIE) Conference Series*, Vol. 4012, *X-Ray Optics, Instruments, and Missions III*, ed. J. E. Truemper & B. Aschenbach, 2–16
- Wesemael, F. 1979, *Astronomy and Astrophysics*, 72, 104
- Wickramasinghe, D. T. & Ferrario, L. 2000, *PASP*, 112, 873
- Williams, K. A., Hermes, J. J., & Vanderbosch, Z. P. 2022, *ApJ*, 164, 131
- Woodgate, B., Kimble, R., Bowers, C., et al. 1998, *PASP*, 110, 1183
- Wu, C., Xiong, H., & Wang, X. 2022, *MNRAS*, 512, 2972
- Wynn, G. A., King, A. R., & Horne, K. 1997, *MNRAS*, 286, 436
- Xu, S., Zuckerman, B., Dufour, P., et al. 2017, *ApJ*, 836, L7
- Yang, H.-W., Thomas Tam, P.-H., & Yang, L. 2022, *RAA*, 22, 105014
- Zhao, L. B. 2021, *ApJS*, 254, 21
- Zhao, L. B. & Liu, F. L. 2021, *MNRAS*, 507, 2283
- Zhong, Y., Kashiwara, K., Takasao, S., Shigeyama, T., & Fujisawa, K. 2023, *The optically thick rotating magnetic wind from a massive white dwarf merger product – II. axisymmetric magnetohydrodynamic simulations*
- Zuckerman, B., Koester, D., Melis, C., Hansen, B. M., & Jura, M. 2007, *ApJ*, 671, 872
- Zuckerman, B., Koester, D., Reid, I. N., & Hüsch, M. 2003, *ApJ*, 596, 477
- Zuckerman, B., Melis, C., Klein, B., Koester, D., & Jura, M. 2010, *ApJ*, 722, 725

<sup>1</sup> Institute of Science and Technology Austria, Am Campus 1, 3400, Klosterneuburg, Austria

<sup>2</sup> Division of Physics, Mathematics and Astronomy, California Institute of Technology, Pasadena, CA91125, USA

<sup>3</sup> Mathematical Sciences Institute, Australian National University, Hanna Neumann Building 145, ACT2601, Canberra, Australia

<sup>4</sup> International Center for Radio Astronomy Research, Curtin University, GPO Box U1987, Perth, WA 6845, Australia

<sup>5</sup> Center for Astrophysics — Harvard & Smithsonian, 60 Garden St., Cambridge, MA 02138, USA

<sup>6</sup> Department of Physics and Astronomy, University of British Columbia, Vancouver, BC V6T 1Z1, Canada

<sup>7</sup> Department of Astronomy, Boston University, 725 Commonwealth Ave., Boston, MA 02215, USA

<sup>8</sup> TAPIR, Mailcode 350-17, California Institute of Technology, Pasadena, CA 91125, USA

<sup>9</sup> Anton Pannekoek Institute for Astronomy, University of Amsterdam, NL-1090 GE Amsterdam, the Netherlands

<sup>10</sup> Department of Physics, Massachusetts Institute of Technology, Cambridge, MA 02139, USA

<sup>11</sup> Department of Physics, University of Warwick, Gibbet Hill Road, Coventry CV4 7AL, UK

<sup>12</sup> University of Washington, Department of Astronomy, Box 351580, Seattle, WA 98195, USA

<sup>13</sup> Max-Planck-Institut für Astrophysik, Karl-Schwarzschild-Str 1, D-85748 Garching, Germany

<sup>14</sup> IPAC, California Institute of Technology, 1200 E. California Blvd, Pasadena, CA 91125, USA

<sup>15</sup> Caltech Optical Observatories, California Institute of Technology, Pasadena, CA 91125, USA

<sup>16</sup> Hamburger Sternwarte, University of Hamburg, Gojenbergsweg 112, 21029 Hamburg, Germany

<sup>17</sup> Grupo de Evolución Estelar y Pulsaciones, Facultad de Ciencias Astronómicas y Geofísicas, Universidad Nacional de La Plata, CONICET-IALP, Paseo del Bosque s/n, 1900 La Plata, Argentina

<sup>18</sup> Departament de Física, Universitat Politècnica de Catalunya, c/Esteve Terrades 5, 08860 Castelldefels, Spain

<sup>19</sup> Leibniz-Institut für Astrophysik Potsdam (AIP), An der Sternwarte 16, 14482 Potsdam, Germany

**Appendix A: HST, XMM-Newton and Chandra X-ray Observations**

Instrument	Mode	Start	End	Duration(s)
COS	TIME-TAG	2022-08-02 14:18:46	2022-08-02 14:56:34	2268.192
COS	TIME-TAG	2022-08-02 15:46:05	2022-08-02 16:30:58	2693.184
COS	TIME-TAG	2022-09-17 10:22:44	2022-09-17 11:00:32	2268.192
COS	TIME-TAG	2022-09-17 11:50:02	2022-09-17 12:34:55	2693.216
STIS	TIME-TAG	2023-08-19 02:21:44	2023-08-19 02:57:07	2122.952
STIS	TIME-TAG	2023-08-19 03:46:22	2023-08-19 03:52:37	374.639
STIS	TIME-TAG	2023-08-19 05:22:07	2023-08-19 06:06:31	2664.097
STIS	TIME-TAG	2023-09-10 09:34:32	2023-09-10 10:18:56	2664.097
STIS	TIME-TAG	2023-09-10 11:09:35	2023-09-10 11:53:59	2664.097
STIS	TIME-TAG	2024-06-23 10:08:55	2024-06-23 10:42:13	1998.072

Table A.1: Table of HST observations of J1901. Total COS exposure time was **9922.784s**. Total STIS exposure time was **12023.952s**.

Instrument	Mode	Filter	Start	End	Duration(s)
XMM EPIC					
MOS1	Large Window	THIN1	2024-03-21 13:51:28	2024-03-22 10:02:02	72634
MOS2	Large Window	THIN1	2024-03-21 13:51:53	2024-03-22 10:05:17	72804
pn	Full Frame	THIN1	2024-03-21 14:17:10	2024-03-22 10:26:30	72560
XMM OM					
OM	Fast	UVW1	2024-03-21 13:59:50	2024-03-21 15:13:10	4400
OM	Fast	UVW1	2024-03-21 15:33:17	2024-03-21 16:46:37	4400
OM	Fast	UVW1	2024-03-21 16:51:44	2024-03-21 18:05:04	4400
OM	Fast	UVW1	2024-03-21 18:10:11	2024-03-21 19:23:32	4401
OM	Fast	UVW1	2024-03-21 19:28:38	2024-03-21 20:41:57	4399
OM	Fast	UVW1	2024-03-21 20:47:05	2024-03-21 22:00:25	4400
OM	Fast	UVW1	2024-03-21 22:05:32	2024-03-21 23:18:51	4399
OM	Fast	UVW1	2024-03-21 23:24:00	2024-03-22 00:05:39	2499
OM	Fast	UVM2	2024-03-22 00:10:46	2024-03-22 01:24:05	4399
OM	Fast	UVM2	2024-03-22 01:29:13	2024-03-22 02:42:33	4400
OM	Fast	UVM2	2024-03-22 02:47:41	2024-03-22 04:00:59	4398
OM	Fast	UVM2	2024-03-22 04:06:07	2024-03-22 05:19:27	4400
OM	Fast	UVM2	2024-03-22 05:24:34	2024-03-22 06:37:54	4400
OM	Fast	UVM2	2024-03-22 06:43:02	2024-03-22 07:56:20	4398
OM	Fast	UVM2	2024-03-22 08:01:27	2024-03-22 09:14:46	4399
OM	Fast	UVM2	2024-03-22 09:19:54	2024-03-22 10:33:14	4400
Chandra					
ACIS-I	VFAINT/TE	-	2022-12-09 14:35:08	2022-12-09 16:56:39	14910
ACIS-I	VFAINT/TE	-	2022-12-10 00:38:11	2022-12-10 02:58:31	14420
ACIS-I	VFAINT/TE	-	2022-12-10 10:33:10	2022-12-10 12:11:29	9980

Table A.2: Table of *XMM-Newton* (EPIC and OM; ObsID 0922750101; PI Traulsen) and *Chandra* (ACIS-I; Proposal ID 24200244) observations of J1901. Total EPIC MOS1 exposure: **72.6** ks, MOS2: **72.8** ks, pn: **72.5** ks. OM total UVM1: **32.9** ks, UVM2: **35.3** ks. ACIS-I total: **39.3** ks.

## Appendix B: X-ray counts

Table B.1: Event counts and statistics for XMM EPIC instruments; PN, M1 and M2. The net source (src) counts are those measured in the 20 arcsec source aperture (without background subtraction). The expected background (bkg) counts are the measured background counts in the 80 arcsec aperture, scaled to the source aperture size. The 90% confidence limits (CL) on the source count rates are shown, with associated detection significance. The PN, M1, and M2 effective exposure times after selection of good time intervals (GTI) are 53.1, 65.1, and 67.3 ks, respectively.

Instr.	Band	src	bkg	CL <sub>90</sub> <sup>low</sup>	CL <sub>90</sub> <sup>high</sup>	Sig.
Instr.	[keV]	[cts]	[exp. cts]	[10 <sup>-4</sup>	cts/s]	$\sigma$
PN	0.2–0.5	117	46.1	10.2	16.9	10.45
	0.5–2.0	147	69.3	11.0	18.6	9.33
	2.0–4.5	42	24.7	1.4	5.4	3.49
	4.5–7.5	31	24.2	0.0	2.9	1.37
	0.2–4.5	306	140.1	26.0	36.8	14.02
M1	0.2–0.5	17	9.7	0.2	2.3	2.33
	0.5–2.0	48	21.5	2.5	6.0	5.72
	2.0–4.5	13	10.0	0.0	1.4	0.96
	4.5–7.5	5	6.8	0.0	0.7	–
	0.2–4.5	78	41.2	3.6	8.0	5.74
M2	0.2–0.5	31	7.3	2.3	5.0	8.75
	0.5–2.0	60	23.9	3.6	7.4	7.39
	2.0–4.5	14	8.6	0.1	1.8	1.84
	4.5–7.5	8	9.0	0.0	0.8	–
	0.2–4.5	105	39.8	7.3	12.3	10.33

Table B.2: Event counts and statistics for the Chandra ACIS-I observation. The net source (src) counts are those measured in the 2.0 arcsec source aperture (without background subtraction). The expected background (bkg) counts are the measured background counts in the 80 arcsec aperture, scaled to the source aperture size. The 90% confidence limits (CL) on the source count rates are shown, with associated detection significance. The ACIS-S total exposure time is 39.3 ks.

Instr.	Band	src	bkg	CL <sub>90</sub> <sup>low</sup>	CL <sub>90</sub> <sup>high</sup>	Sig.
Instr.	[keV]	[cts]	[exp. cts]	[10 <sup>-5</sup>	cts/s]	$\sigma$
ACIS-I	0.2–0.5	0	0.01	0.0	5.9	–
	0.5–1.2	1	0.05	0.1	9.8	1.6
	1.2–2.0	6	0.06	6.9	28.0	6.5
	0.5–2.0	7	0.11	8.5	31.2	6.5
	2.0–7.0	3	0.23	1.8	17.1	2.9
	0.5–7.0	10	0.33	13.5	40.4	6.9

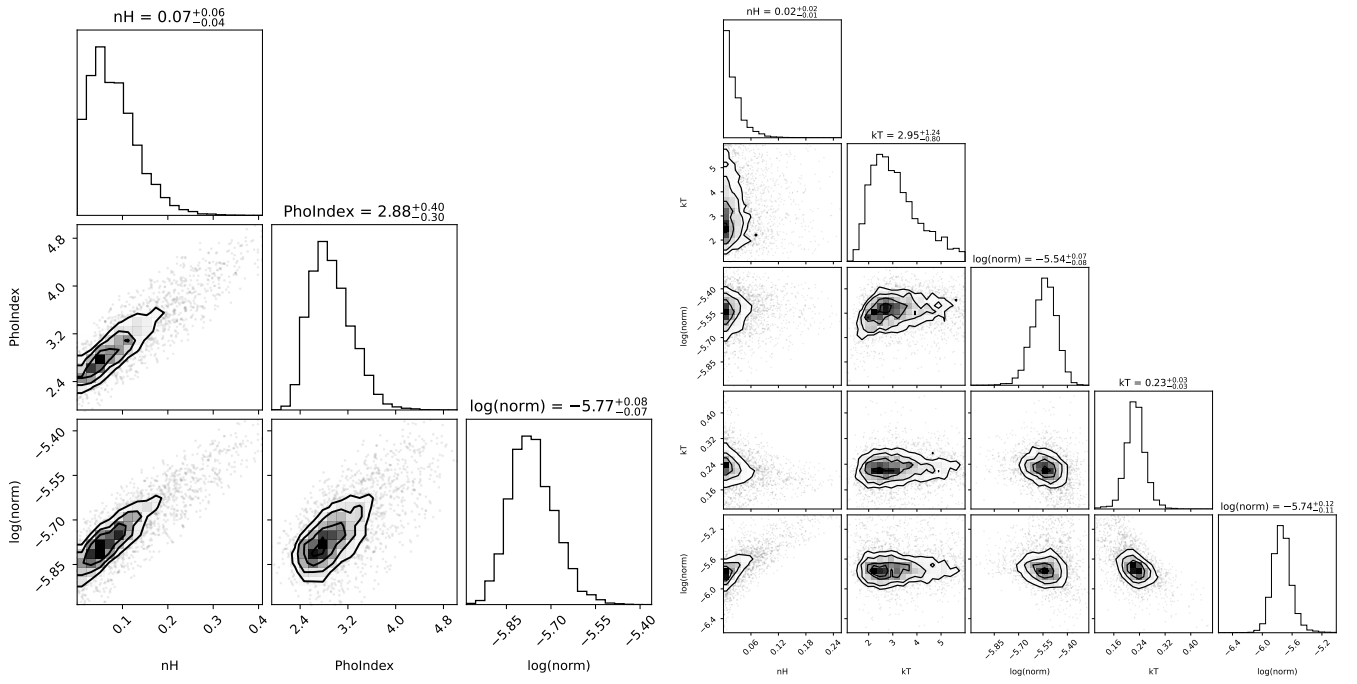


Fig. B.1: **Left:** Posterior distributions of the three parameters included in the X-ray spectral fitting of the power law model. **Right:** Posterior distributions of the five parameters included in the X-ray spectral fitting of the two-temperature, optically-thin plasma model.